Recovery of sparse urban greenhouse gas emissions

Benjamin Zanger[1], Jia Chen[1], Man Sun[1], and Florian Dietrich[1]

[1]Environmental Sensing and Modeling, Technical University of Munich (TUM), Munich, Germany

Correspondence: Benjamin Zanger (benjamin.zanger@tum.de) and Jia Chen (jia.chen@tum.de)

Abstract. To localize and quantify greenhouse gas emissions from cities, gas concentrations are typically measured at a small number of sites and then linked to emission fluxes using atmospheric transport models. Solving this inverse problem is challenging because the system of equations often has no unique solution and the solution can be sensitive to noise. A common top-down approach for solving this problem is Bayesian inversion with the assumption of a multivariate Gaussian distribution as the prior emission field. However, such an assumption has drawbacks when the assumed spatial emissions are incorrect or not Gaussian distributed. In our work, we investigate sparse reconstruction (SR), an alternative reconstruction method that can achieve reasonable estimations without using a prior emission field by making the assumption that the emission field is sparse. We show that this assumption is generally true for the cities we investigated and that the use of the discrete wavelet transform helps to make the urban emission field even more sparse. To evaluate the performance of SR, we created concentration data by applying an atmospheric forward transport model to CO_2 emission inventories of several major European cities. We used SR to locate and quantify the emission sources by applying compressed sensing theory and compared the results to regularized least squares (LS) methods. Our results show that SR requires fewer measurements than LS methods and that SR is better at localizing and quantifying unknown emitters.

1 Introduction

Understanding anthropogenic greenhouse gas (GHG) emissions is important for scientists and decision makers fighting climate change. Based on a growing amount of atmospheric observations, studies estimating emission fields of GHG sources and sinks from these observations have been performed on local (Chen et al. (2016); Viatte et al. (2017); Toja-Silva et al. (2017)), metropolitan (Jones et al. (2021); Turner et al. (2020); Hase et al. (2015)), country (Miller et al. (2013); Shekhar et al. (2020)), and global (Hirsch et al. (2006); Mueller et al. (2008); Turner et al. (2015); Jacob et al. (2016)) scale. One of the main reason for such studies is to verify and improve GHG emission inventories created by bottom up methods. Verification and improvements include, but are not limited to:

– Determining the difference between the real emissions and the emissions captured by inventories.

– Determining differences between the real and bottom up estimated emissions for individual emitters.

– Finding emitters which are not captured by inventories (unknown emitters).

25   Atmospheric inverse modeling methods use column or in situ GHG concentration measurements to estimate emission fields. Due to a lack of measurements and high modeling and measurement uncertainties, estimating each grid cell of an emission field independently is not possible. Instead, sectors (Jones et al., 2021), spatial correlations (Wesloh et al., 2020), and/or temporal correlations (Jones et al., 2021; Wesloh et al., 2020) are used to construct alternative parameterizations of emission fields to prevent overfitting.

30   An alternative to overcome these issues are sparse reconstruction (SR) methods (Ray et al., 2015). SR methods can use concentration measurements to estimate sparse emission fields, meaning that only a small number of large emitters contribute significantly to the total emissions. These methods determine the critical emission grid cells and adjust the emissions of only those cells until the model best matches the observations. All other grid cells are set to zero. Once conditions of compressed sensing (CS) are fulfilled, SR methods are guaranteed to determine the best possible emission fields and provide a good

35   estimation of their emissions.

SR for the recovery of GHGs has been proposed by several recent studies. Ray et al. (2014, 2015) used stagewise orthogonal matching pursuit (StOMP), a reconstruction method known from compressed sensing, and modified it to enforce positive emission estimates. To overcome the restriction of sparse reconstruction of only being able to reconstruct sparse fields, they used a multi scale resolution field based on wavelets. In Ray et al. (2015), StOMP has been modified so that prior information

40   can be included. Both studies reconstructed fossil fuel CO_2 emissions in an idealized scenario with synthetic measurements and very low measurement noise (SNR $> 40\,\mathrm{dB}$). Hase et al. (2017) demonstrated sparse reconstruction with enforced positive emissions estimates of anthropogenic CH_4 emissions from synthetic observations in the US. To increase the sparsity of the emission field, Hase et al. (2017) used a redundant dictionary representation, where the representation of the emission field is not unique. Yan et al. (2012) proposed compressed sensing, i.e. sparse reconstruction with guaranteed best feature selection,

45   for environmental monitoring with the focus on undersampling.

In this paper, we apply SR for assessing urban GHG emissions. Current GHG emission monitoring systems in cities, such as Dietrich et al. (2021); Shusterman et al. (2016) and Sargent et al. (2018), acquire GHG concentration in the atmosphere as column or in situ concentration measurements. These measurements are then related to city emissions and background concentrations, where the city emissions are the unknowns of interest while the background is (partially) known. Göckede

50   et al. (2010) have shown that on smaller domains, uncertainties in the background has a high influence on the estimation of the city emissions. Therefore, modern approaches, such as Jones et al. (2021) and Klappenbach et al. (2021), use the measurements acquired to additionally improve the certainty of background concentrations using a Bayesian approach. In this work, we ignore the background and make the assumption that it is known in full detail. Extending our approach to include background concentrations is straightforward.

55   As urban emissions, we are using anthropogenic emission inventories from multiple European cities. To overcome the sparsity constraints of SR for non-sparse emissions, we use a wavelet transformation.

We are the first to apply SR to the estimation of urban GHG emissions. The findings of our work are the following:

– Urban emissions are mostly sparse and a 3rd level wavelet transform performs well in sparsifying urban emissions further.

– SR needs less measurements than Gaussian prior methods to achieve a similar performance if the emissions are sparse enough.

– SR performs well on localizing and quantifying large emitters, leading to the application of finding unknown emitters not captured by emission inventories.

The paper is structured as following: Sec. 2 gives a formulation of inverse problems, introduces the reader to sparse reconstruction methods, compressed sensing, and compressible emissions and provides a discription of the algorithms used in this paper. The compressability of the anthropogenic emissions in European cities is discussed in Sec. 3. Section 4 shows selected scenarios of our reconstruction method, highlighting beneficial conditions and use cases of our reconstruction method, as well as discussing measurement noise. In Sec. 5 we create case studies for different European cities in an idealized and noisy case.

2 Methodology

This section gives the problem statement of atmospheric inverse problems (Sec. 2.1), provides an introduction to the theory of sparse reconstruction (Sec. 2.2, Sec. 2.3, and Sec. 2.4), and introduces measures (Sec. 2.5) and algorithms (Sec. 2.6) for sparse reconstruction.

2.1 Inverse Problems

An inverse problem is a problem in which input parameters should be determined from the observation of a process. For the problem in this paper, those input parameters $x \in \mathbb{R}^n$ are the GHG emission fluxes for each grid cell in an emission field and the measurements $y \in \mathbb{R}^m$ are in situ or column measurements of GHG concentrations in the atmosphere. These quantities are connected by an atmospheric process, referred to as forward model F, $y = F(x)$. In practice, such a forward model can be a linear, non-linear, or even a stochastic process. For this analysis, we limit the forward model to linear cases. Therefore, we can write $y = Ax$, where $A \in \mathbb{R}^{m \times n}$ is called the sensing matrix. A least squares estimation of the GHG emission fluxes x is given by

$$\hat{x} = \underset{x}{\arg\min} \|Ax - y\|_2^2. \tag{1}$$

Often, however, such inverse problems are ill-posed, as in the cases we deal with in this paper. In such cases, no or no unique solution exists or the solution does not depend smoothly on the data, therefore, being sensitive to noise. For ill-posed inverse problems, the least squares estimation without regularization does not provide a useful reconstruction technique. For a more detailed discussion of ill posed problems we refer to chapter 3 of Nakamura and Potthast (2015).

2.2 Bayesian Inversion

A typical approach in atmospheric sciences to solve inverse problems is Bayesian inversion. In such a setup, the unknown emissions are assumed to follow a known probability distribution. This probability distribution is referred to as a priori. Measurements are used to update the a priori, which results in a new probability distribution referred to as a posteriori. From this

posteriori distribution a parameter estimation can be made using a maximum likelihood (ML) detector on the a posteriori. Since the ML detector acts on the a posteriori, this is commonly referred to as Maximum a posteriori (MAP) detector. Let us call the probability distribution of the a priori $p_X(x)$. Furthermore, probability distributions are assigned both to the observations and the model to account for uncertainties. The measurement distribution is written as $p_Y(y)$ and the distribution which maps x to y is written as $p_{Y|X}(y|x)$. Using Bayes' theorem, a posteriori distribution for x under the condition of the observations y can be derived:

$$p_{X|Y}(x|y) = \frac{p_{Y|X}(y|x)p_X(x)}{p_Y(y)}. \tag{2}$$

On this derived distribution the MAP detector can be applied. Since $p_Y(y)$ is only a constant factor for some specific measurements, the MAP detector can be written as

$$\hat{x} = \arg\max_x \ p_{Y|X}(y|x)p_X(x), \tag{3}$$

where $\hat{x}$ are the estimated physical quantities. Typically the distributions are assumed to be Gaussian, where the a priori distribution is assumed to be centered around an initial guess, x_A. This allows for easier error analysis and makes the problem computationally feasible.

2.3 From Bayesian Inversion to Regularization

To show the relation between Bayesian inversion and regularization methods, we show how a Bayesian inversion problem, using Gaussian priors, can be converted to a regularization problem. Assume that $p_{Y|X}(y|x)$ is Gaussian distributed with the covariance matrix S_o,

$$p_{Y|X}(y|x) = \frac{1}{\sqrt{(2\pi)^m \det(S_o)}} \exp\left(-\frac{1}{2}\left\|S_o^{-1/2}(Ax - y)\right\|_2^2\right), \tag{4}$$

where m are the number of measurements, and $p_X(x)$ to be a Gaussian prior of the form

$$p_X(x) = C\exp\left(-\frac{1}{2}\left\|S_A^{-1/2}(x - x_A)\right\|_2^2\right), \tag{5}$$

where C is a normalization constant. Applying the MAP detector from Eq. (3) gives an estimation of

$$\hat{x} = \arg\max_x \ p_{Y|X}(y|x)p_X(x) \tag{6}$$

$$= \arg\min_x \left[\left\|S_o^{-1/2}(Ax - y)\right\|_2^2 + \left\|S_A^{-1/2}(x - x_A)\right\|_2^2\right]. \tag{7}$$

The idea of regularization methods on the other hand is to add a penalty term to the least squares problem from Eq. (1) to prefer solutions of a certain kind,

$$\arg\min_x \left[\left\|C_1\left(Ax - y\right)\right\|_2^2 + \lambda R(C_2 x)\right], \tag{8}$$

where $R : \mathbb{R}^n \to \mathbb{R}$ is the regularization function and C_1, C_2 are correlation matrices. This equation is equivalent to Eq. (6) with $\lambda = 1$, $C_1 = S_o^{-1/2}$, $R = \left\| S_A^{-1/2}(x - x_A) \right\|_2^2$, and $C_2 = 1$. For such a regularization function, the regularization scheme is known as Tikhonov regularization or also ridge regression (Golub et al., 1999). While in Bayesian inversion it is most often assumed that a prior value x_A is known, in regularization x_A is often unknown and assumed to be 0.

In this paper, we investigate sparse reconstruction (SR) methods. To achieve SR, the regularization term has to be changed so that sparse solutions are preferred over non-sparse solutions. In statistics, such a regularization function is the Lasso regularization function, presented by Tibshirani (1996). The Lasso is given by

$$R(x) = \sum_j |x_j| = \|x\|_1 \tag{9}$$

and is used especially when x is approximately sparse. The equivalent of the Lasso in Bayesian inversion is the assumption of a Laplacian distributed prior. The Lasso is expected to select those elements in x which are important and meaningful, while the irrelevant features are estimated to be zero. Su et al. (2017) showed that this is not necessarily the case, as coefficients which are zero in x are sometimes estimated to be important (which is referred to as false discovery). In the next section, we introduce compressed sensing (CS), which provides sufficient conditions to prevent false discoveries in x using Lasso regularization.

2.4 Compressed Sensing

Compressed sensing (CS) is a theory which provides sufficient conditions to guarantee best possible reconstruction using the Lasso regularizer, therefore, preventing false discoveries. The conditions of CS apply to the forward model A and are hard to examine. For this reason, the conditions are normally already considered in the design process. In the following, we provide the very basics of CS needed to understand our work. For a more comprehensive introduction to CS, we refer to Boche et al. (2015).

CS states that an s-sparse signal $x \in \Sigma_s^n$, where s-sparse is defined as $s \geq |\{j | x_j \neq 0\}|$ and Σ_s^n is the set of all s-sparse signals which are in $\mathbb{R}^n$, can be uniquely reconstructed by m measurements $y \in \mathbb{R}^m$, defined by $y = Ax$, where $A \in \mathbb{R}^{m \times n}$, if certain conditions are satisfied for A. An overview of the symbols, norms, and measures used is given in Table 1. The unique solution is found by solving the l_0 minimization problem given by

$$\hat{x} = \arg\min_x \|x\|_0 \text{ s.t. } Ax = y. \tag{P0}$$

Solving this minimization problem is NP-hard and not applicable to real world applications. Candès et al. (2006) showed that for additional conditions in A, one can solve the l_1 regularization problem instead, which is a convex problem:

$$\hat{x} = \arg\min_x \|x\|_1 \text{ s.t. } Ax = y. \tag{P1}$$

Then, solving Eq. (P1) leads to the same solution as Eq. (P0). A sufficient condition for recovering (P0) with (P1) is the Restricted Isometry Property (RIP) introduced in Candès and Tao (2005). This property determines a Restricted Isometry Constant (RIC) δ_s for a certain sparsity level s, which is calculated by

$$(1 - \delta_s)\|x\|_2^2 \leq \|Ax\|_2^2 \leq (1 + \delta_s)\|x\|_2^2, \tag{10}$$

where $x \in \Sigma_s^n$. The RIC tells how close the singular values of $m \times s$ submatrices of A are to 1. For $\delta_{2s} < 1$, any s-sparse solution can be uniquely determined by solving the (P1) problem and for $\delta_{2s} < (\sqrt{2} - 1)$ this is even possible if the signal is superimposed by noise (noisy case) (Candès, 2008). In practice, calculating the RIC is NP-hard (see Tillmann and Pfetsch (2014)) and it is not applicable to calculate this constant for a given matrix. However, the RIP might be used within a design process, since there are known random distributions of matrices, which satisfy the RIP for large s considering sufficient large n and m (Baraniuk et al., 2008). Another property, which very loosely upper bounds the RIC, is the incoherence property (Wang et al., 2015). The coherence μ of a matrix is defined by

$$\mu = \max |< a_i | a_j >| \qquad i \neq j, \tag{11}$$

where a_i and a_j are distinct column vectors of $\tilde{A}$, where $\tilde{A}$ is the column normalized matrix of A. The coherence bounds the RIC by

$$\delta_{2s} \leq (2s - 1)\mu. \tag{12}$$

Therefore, s-sparse solutions can be uniquely recovered if $\mu < \frac{1}{2s-1}$ holds in the noiseless case or $\mu < \frac{\sqrt{2}-1}{2s-1}$ in the noisy case.

In real world scenarios, coefficients are rarely sparse but often compressible. This means that the coefficients can be well approximated by sparse coefficients. A more detailed explanation for compressible coefficients is found in Sec. 2.5. CS guarantees good estimates of compressible solutions if the RIP is satisfied for the noisy case. Then the reconstruction error can also be bounded (see Candès (2008) for the exact definitions and bounds).

2.5 Sparsifying Emissions

Sparsity is one of the key elements for SR. However, emissions are not always sparse. In order to make a non sparse emission field sparse, a transformation into a different domain can be used. Such transformations include the Fourier transform, wavelet transform, transformations tailored to specific data sets, e.g. by SVD truncation (see Hong et al. (2011)), or overcomplete dictionaries, where the representation does not have to be orthogonal and multiple representations for the same emission field exist (see Candès et al. (2011)). In this paper, we only deal with the discrete wavelet transform (DWT) to sparsify emissions. This transform is used for image compression (Lewis and Knowles, 1992) and was also used in Ray et al. (2014) and Ray et al. (2015) to parameterize fossil fuel CO_2 emissions for the US.

There are several ways to quantify the sparsity of an emission field. One possibility is to measure the error, using any l_p norm, of an emission field x to its best s sparse approximation,

$$\sigma_s(x)_p = \inf \left\{ \|x - z\|_p, z \in \Sigma_s^n \right\}. \tag{13}$$

Independent of the norm used, the best approximation is given by an emission field z, which contains the same s highest values of x and is zero otherwise. Often, it is more intuitive to give the relative sparsity s_{rel}, which is the fraction of non zero entries as a percentage of all entries, instead of the sparsity level s. In this paper, both notations are used, e.g. $\sigma_{10\%}(x)_2$ is the l_2 error of the signal which best approximates x and maximally possesses 10 % non zero elements while $\sigma_{10}(x)_2$ is the l_2 error of the

signal approximating x with maximally 10 non zero elements. To show the distribution of values in x, a plot showing $\sigma_s(x)$ over all possible s can be used. An example is depicted in Fig. 1. The more hyperbolic the plot is, the more compressible the
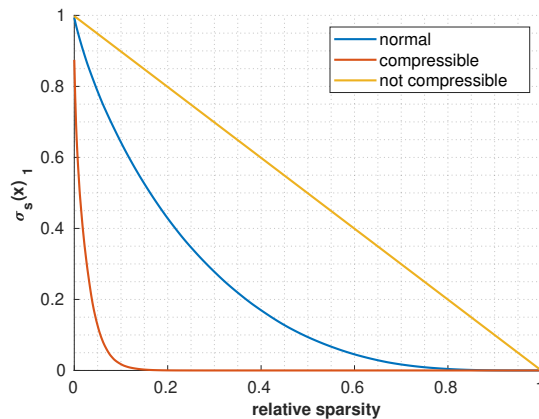
Figure 1. Visualization of the compressability of emission fields by plotting $\sigma_s(x)_1$ over all s. The more hyperbolic the curve is, the more compressible the emission field.

signal is. In order to get a measure for the compressability of the distribution, the Gini index is used, which was also proposed as a sparsity measure for CS by Zonoobi et al. (2011). This index measures how unequal x is distributed, which is a similar measure as the hyperbolicity of a curve in the depicted figure. For the case of an equal distribution (yellow curve) the Gini index becomes 0 and for a highly compressible distribution (orange curve) the Gini index gets close to 1. A Gini index of exactly 1 is equal to a 1-sparse signal.

In this paper, a DWT is used to sparsify emissions, using Haar wavelets. Throughout the paper, we use the 3rd level wavelet transform and refer to its matrix as W and its inverse transformation as W^{-1}. For an introduction to wavelets, we refer to Graps (1995) and Mallat (1999). For the visualization of a 3rd level DWT, see Fig. 1.1 in Mallat (1999). The emission map x is transformed into its wavelet coefficients c by $Wx = c$ and vice versa by $x = W^{-1}c$. To transform the forward model $Ax = y$ into the wavelet domain, we write

$$y = Ax = AW^{-1}c = \bar{A}c, \tag{14}$$

where $\bar{A} = AW^{-1}$ is the new forward model. The wavelet coefficients are then determined by the modified (P1) problem,

$$\hat{c} = \arg\min_{c} \|c\|_1 \text{ s.t. } \bar{A}c = y. \tag{15}$$

Note that the CS conditions for $\bar{A}$ are not the same as for A. Once the wavelet coefficients $\hat{c}$ are determined, the emissions are estimated by $\hat{x} = W^{-1}\hat{c}$.

2.6   Reconstruction Algorithms

195   There have been many algorithms proposed for the task of CS and SR. However, our goal in this paper is not to compare these algorithms, instead, we want to demonstrate the applicability of SR in general for urban GHG emission assessments. We, therefore, only solve the initial SR problem, given in Eq. (P1). To find the minimum, we use the cvx library, a matlab package for specifying and solving convex programs (Grant and Boyd (2014, 2008)), using the gurobi optimizer as a backend (Gurobi Optimization, LLC, 2021).

200   For the noisy case, we solve a modified form of Eq. (P1), given by

$$\hat{x} = \arg\min_x \|x\|_1 \text{ s.t. } \|Ax - y\|_2^2 \leq \|\epsilon\|_2^2, \tag{P1ϵ}$$

where ϵ is the noise vector. This is equivalent to the Lasso with the right choice of λ. Since we generate the noise by design, the optimization process simplifies by choosing ϵ without having to find the right λ value.

We compare our results to regularized least squares, which we refer to as least squares (LS) hereafter. The equation of the
205   LS is given by

$$\hat{x} = \arg\min_x \|x\|_2 \text{ s.t. } Ax = y, \tag{P2}$$

in the noiseless case. There, the solution is given by the pseudoinverse. In the noisy case, the equation is given by

$$\hat{x} = \arg\min_x \|x\|_2 \text{ s.t. } \|Ax - y\|_2^2 \leq \|\epsilon\|_2^2. \tag{P2ϵ}$$

2.7   Data Evaluation

210   Table 1 gives an overview of the most important symbols and measures used in this paper. All of the measures we are using for evaluating the reconstruction results compare the estimations to the true emissions, which are the city emission inventories in this paper. If the l_p error is not specified, the l_2 error is used. The primary measure we use for the error evaluation of our estimates is the relative l_2 error, since it provides a measure for the highest spatial resolution of the emissions (1 km $\times$ 1 km), while the relative l_2 smoothed error shows an error for a lower spatial resolution (5 km $\times$ 5 km) and eliminates errors which
215   are due to spatial errors. Because of the high spatial resolution of the emission fields reconstructed in this paper, relative l_2 error values greater then 1 are possible. Those are because of spatial errors, where an emission is assigned to the wrong spatial location. The relative total error disregards these spatial errors and only evaluates the difference of the total estimated emission to the true total emission of a city.

The mean relative error is used if the relative error of emission grid points independent of their contribution to the total
220   amount of emissions is of interest. This metric is useful to evaluate how well a reconstruction method estimates emitters of a certain kind.

Table 1. Table of symbols and measures used in the paper.

Expression	Formulation	Explanation
Norms		
l_p norm	$\left(\sum_i x_i^p\right)^{\frac{1}{p}}$	l_p norm for vectors $x \in \mathbb{R}^n$.
l_0 norm	$|\{j\|x_j \neq 0\}|$	Number of non zero elements in x.
Symbols		
n	$\dim(x)$	Number of unknown emissions in the model.
m	$\dim(y)$	Number of measurements.
s	$\|x\|_0$	Number of non zero entries in x.
relative sparsity / s_{rel}	$\dfrac{\|x\|_0}{\dim(x)}$	Number of non zero entries in $x \in \mathbb{R}^n$, relative to the size of the vector x.
Σ_s^n	$\left\{x\| \|x\|_0 \leq s, x \in \mathbb{R}^n\right\}$	Set of all s sparse vectors in $\mathbb{R}^n$.
Sparsity measures		
$\sigma_s(x)_p$	$\inf\left\{\|x - z\|_p, z \in \Sigma_s^n\right\}$	l_p error of the best possible approximation of the true emissions x by a s sparse emission field z. If s is given in a percentage, s_{rel} instead of s is used.
Measures for evaluating reconstruction results		
relative l_p error	$\dfrac{\|x - \hat{x}\|_p}{\|x\|_p}$	Relative error of how well the estimated emissions $\hat{x}$ approximate the true emissions x.
relative smoothed l_p error	$\dfrac{\|x * \square - \hat{x} * \square\|_p}{\|x * \square\|_p}$	Relative error of smoothed reconstruction, smoothed by a periodic convolution using a 5 km $\times$ 5 km square ($\square$).
relative total error	$\dfrac{\left|\sum_i x_i - \sum_i \hat{x}_i\right|}{\left|\sum_i x_i\right|}$	Relative error of the sum of the estimated emissions $\hat{x}$ compared to the true emissions x.
mean relative error	$\dfrac{1}{n}\sum_{i=1}^n \dfrac{|x_i - \hat{x}_i|}{|x_i|}$	Mean of the relative errors of single emission grid points.

3 The Sparsity/Compressibility of Emissions in European Cities

In the following, we determine the sparsity and compressibility of real world emissions. To do so, we study the CO_2 emissions of major European cities, such as Berlin, Hamburg, Munich, London, Paris, and Vienna using data from the TNO_GHGco_v1.1 emission inventory (van der Gon et al., 2019). This database provides annual grided anthropogenic emissions with a resolution of about 1 km $\times$ 1 km for the areas and species. Furthermore, the emissions are classified by a proxy, such as public power, industry, stationary combustion, etc. Emissions of all proxies of the dataset are included for the emission data used, making the assumption that this provides a good representation of typical emission fields for the cities investigated. We measure the sparsity of the cities using the Gini index and $\sigma_{10\%}(x)_2$ in the spatial and wavelet domain. The results are given in Table 2. For all

225

Table 2. Sparsity of the reported emission fields in different European cities. In the wavelet domain, in all of the cases a better, or at least as good, sparse approximation of the emission map exists.

City	number of emission fields n	Gini index	Gini index DWT	$\sigma_{10\%}(x)_2$	$\sigma_{10\%}(x)_2$ **DWT**
slightly compressible					
London	2205	0.544	0.924	0.359	0.221
Paris	2655	0.673	0.937	0.217	0.150
highly compressible					
Berlin	1554	0.772	0.956	0.070	0.058
Hamburg	1554	0.792	0.956	0.081	0.066
Vienna	750	0.831	0.962	0.070	0.070
Munich	528	0.712	0.956	0.077	0.048

the cities we consider, the wavelet domain of the emission fields achieves a higher Gini index compared to the spatial domain. Furthermore, the approximation error of $s_{\mathrm{rel}} = 10\%$ of the signal is lower in the wavelet domain, except for Vienna, where this error is identical for both domains. From these data, we conclude that a representation of the city emission fields in the wavelet domain should generally be better suited for SR. We also split the cities into two groups, cities whose emission fields are highly compressible (Berlin, Hamburg, Vienna, and Munich, Gini index > 0.7) and cities where the fields are significantly less compressible (London and Paris, Gini index < 0.7).

4 Evaluating Sparse Reconstruction of GHG Emissions

In the following, we define the estimation problem (Sec. 4.1) and apply SR to several European cities (Sec. 4.2).

4.1 Formulating the Estimation Problem

In the following, we assume that the influence of the background GHG concentration on the measurements is fully known. Subtracting this influence from the measurements yields the enhancement produced by the GHG emissions in the domain of interest. Therefore, the background can be ignored and the model is simplified to a pure transport emission system. Let the sensitivity of the GHG concentration measurements y to the city emissions x be given by the sensing matrix A,

$$y = Ax. \tag{16}$$

The rows in A contain vectorized footprints, which determine the sensitivity of the measurements to the GHG fluxes of different emission grid cells in the domain. These footprints are determined by backward transport models, such as the Stochastic Time-Inverted Lagrangian Transport (STILT) model (Lin et al., 2003; Gerbig et al., 2003). In this paper, a simplified linear model,

the Gaussian plume model, is used as the transport model. This approach allows varying parameters within the transport model without the computationally costly calculations of the STILT model. In Appendix B, we explain how the Gaussian plume footprints are created and show two footprints, one calculated by STILT, the other by the Gaussian plume model (Fig. B1). In
250 our work, we use artificial wind data. These wind fields used, except in Sec. 4.2.1, possess a wind coverage of $\sim 143°$. All of the footprints generated by those wind fields are available at https://doi.org/10.5281/zenodo.5901298 (Zanger et al., 2022a).
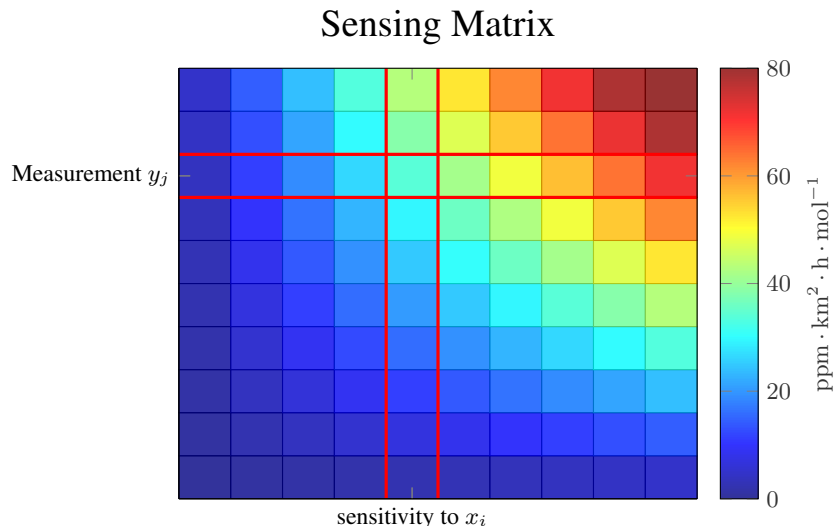
Figure 2. Visualization of a sensing matrix, where the values in the matrix are color encoded. The entry A_{ji} in the matrix gives the sensitivity of the jth measurement to the ith grid cell.

Figure 2 visualizes the sensing matrix A, which represents the sensitivity of all measurements to each grid cell. Depending on the footprints in A, there might be emissions in x which are not strongly sensed. The total sensitivity to a single grid cell x_i is determined by the sum of the corresponding column in the sensing matrix. If this sensitivity is below a certain threshold,
255 $\sum_j A_{ji} \leq \gamma$, where $\gamma = 10^{-9}$ ppm $\cdot$ km^2 $\cdot$ h $\cdot$ mol^{-1} is the threshold, we remove the ith column from the sensing matrix and do not reconstruct this emission grid cell. For Fig. 2 this would be the first column of the sensing matrix, where all values are 0. This introduces some small perturbation between y and Ax, so that $Ax \approx y$. However, since we choose our threshold small enough, this is not reflected in the solution but improves the conditioning of A and reduces the computational effort.

From a physical point of view, these removed emission grid cells are not situated upwind of the measurement stations and,
260 therefore, cannot be well reconstructed using the measurements. For the wavelet domain, we perform this step on the wavelet transformed sensing matrix. Therefore, wavelet coefficients which are weakly sensed and below the threshold are removed.

In our study, we use both artificially created emission fields and real emission fields (van der Gon et al., 2019). Both field types have a spatial resolution of 1 km $\times$ 1 km. For the artificial emissions, a domain size of 32 km $\times$ 32 km is used, resulting in $n = 1024$ unknown emission grids. For the emission inventory, the number of emission grids depends on the size of the city
265 (see Table 2). In order to compare emissions estimates of the different domains, we vary the number of measurement stations
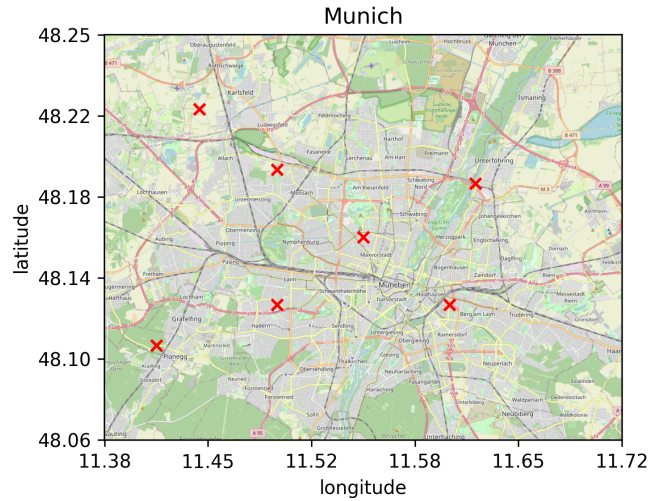
Figure 3. Map of exemplary measurement locations for Munich using seven measurement stations, which represents a ratio $\frac{m}{n}$ of approximately 75 % (background: ©OpenStreetMap contributors 2020. Distributed under the Open Data Commons Open Database License (ODbL) v1.0. (2020)).

used for each domain, so that the number of measurements per unknown emission grid ($\frac{m}{n}$) is roughly constant. During the measurement period, each station takes 50 samples. The measurement stations were randomly distributed over a normalized area of the emission map and scaled to the domain size of each city. An exemplary distribution of the stations for Munich is depicted in Fig. 3, using $\frac{m}{n} \approx 75$ %.

270   The measurements y are then created using the sensing matrix A and the emissions x: $y = Ax$. In the noisy case, we add a Gaussian distributed noise vector to the measurements, $y = Ax + \epsilon$, $\epsilon \sim \mathcal{N}(0, \sigma_\epsilon^2)$. σ_ϵ is chosen based on the SNR used.

4.2   Applying Sparse Reconstruction to European Cities

Reconstruction results for Munich in the noiseless case using LS, SR, and SR in the wavelet domain are depicted in Fig. 4, and the reconstruction errors for the figure can be found in Table 3. A visual inspection indicates, SR in the wavelet domain does

275   resemble the real emissions best, while SR in the spatial domain is second best. Negative emitters are not visible because of the color scale. LS estimates a total of 171 such negative emitters with a total of 2139 $\mu\mathrm{mol} \cdot (\mathrm{m}^2 \cdot \mathrm{s})^{-1}$ negative emissions, while SR estimates only 33 negative emitters with a total of 9 $\mu\mathrm{mol} \cdot (\mathrm{m}^2 \cdot \mathrm{s})^{-1}$ negative emissions. SR in the wavelet domain estimates 50 negative emitters with a total of 59 $\mu\mathrm{mol} \cdot (\mathrm{m}^2 \cdot \mathrm{s})^{-1}$ negative emissions.

     In the following, we identify properties of SR and compare them to the LS using the European city emission inventories.

280   The properties we identify are interconnection between SR and CS (Sec. 4.2.1), the wavelet domain to make emissions sparser (Sec. 4.2.2), the ability of identifying unknown emitters (Sec. 4.2.3), and the number of measurements needed (Sec. 4.2.4). We first analyze these properties in the noiseless case (Sec. 4.2.1 to 4.2.4) and then extend those to the noisy case (Sec. 4.2.5).
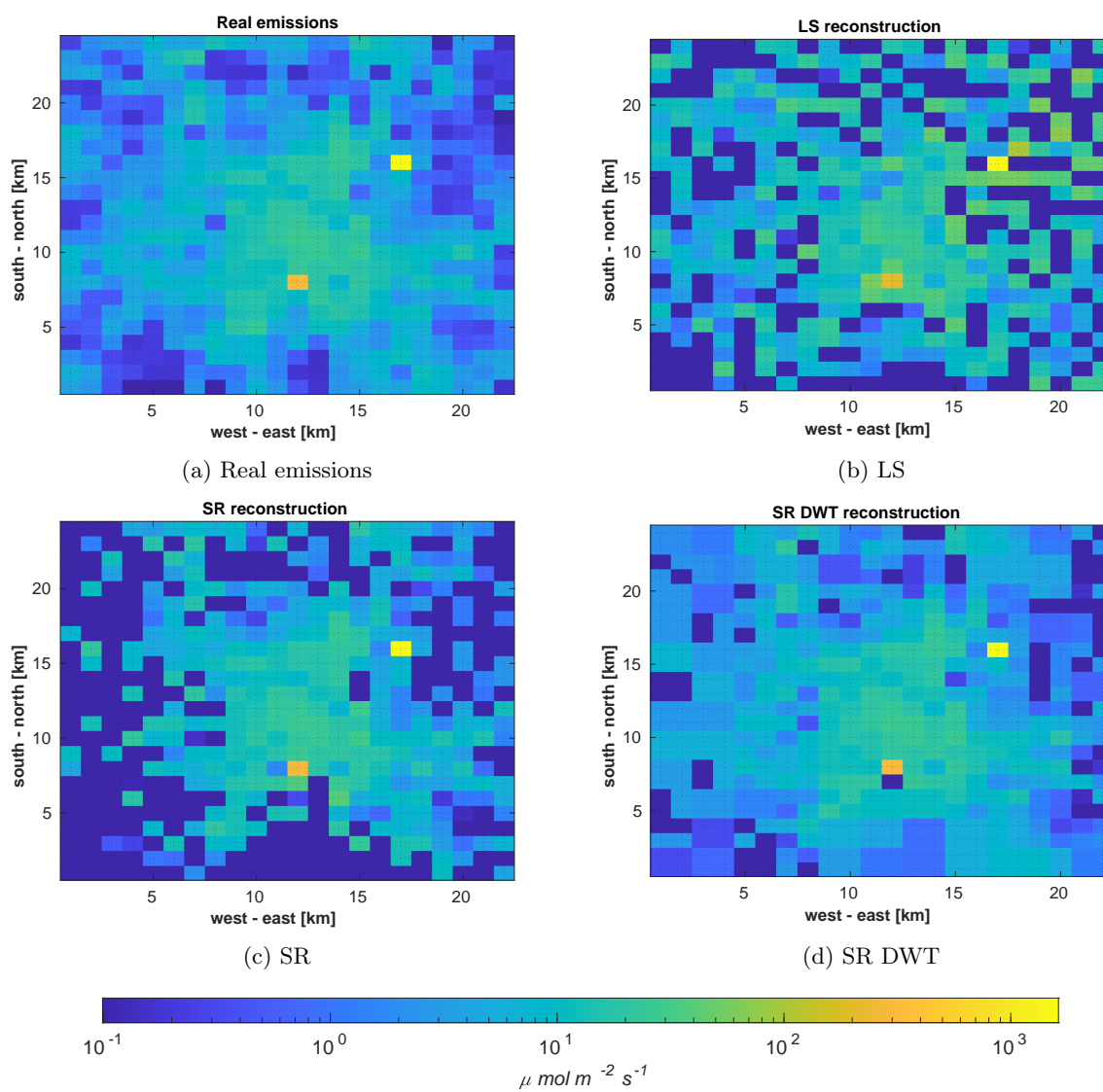
Figure 4. Visualization of the (a) emission inventory of Munich and estimated emission fields of the inventory by using (b) LS, (c) SR, and (d) SR in the wavelet domain. The color scale is logarithmic and given in the unit of $\mu\mathrm{mol} \cdot (\mathrm{m}^2 \cdot \mathrm{s})^{-1}$. Negative emissions are colored dark blue and can not be visually distinguished from low or 0 emitters. The emission inventory does not include negative emitters.

Additionally, in Appendix A, we present an example using artificial, sparse emissions to better establish further connections between SR and CS.

4.2.1 Influence of Wind Coverage

We examine the effect of wind coverage on the effectiveness of the sensing matrix for SR. The term wind coverage is used to measure the range of wind directions during the measurement period. A wind coverage of $0°$ corresponds to no changes in the wind direction during the observations, while a wind coverage of $360°$ means that the wind blew from all directions during the time of observation. The wind coverage is changed in an interval from $96°$ to $360°$, with a step size of $24°$, using a Gaussian
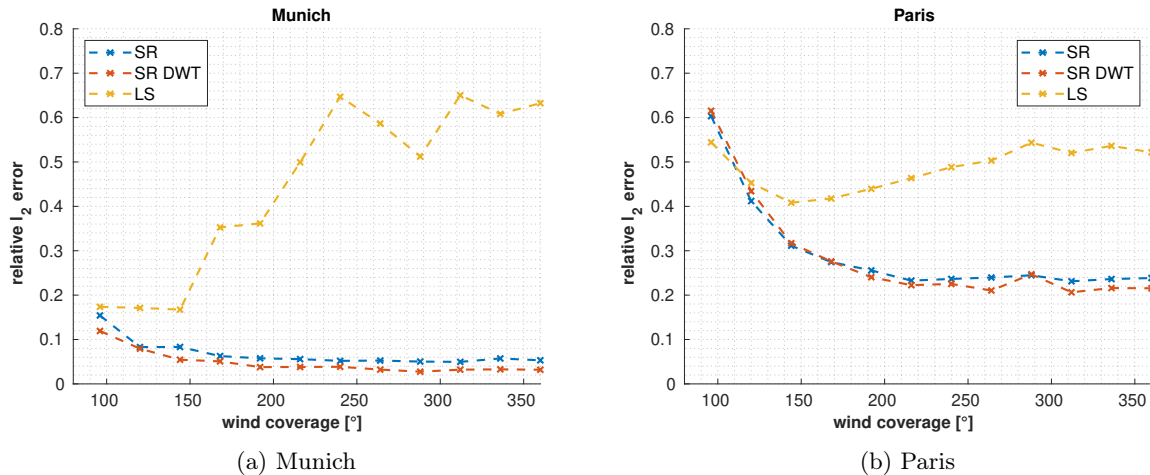
(a) Munich (b) Paris

Figure 5. Estimation errors for SR in the spatial and wavelet domain and LS reconstruction of (a) Munich's and (b) Paris's emissions with footprints covering different amount of wind directions. With a higher wind coverage, the estimation result using SR improves. The LS has no clear improvement for higher wind coverages, but its performance decreases with high coverages for Munich, while for Paris the performance first increases until about a coverage of $150°$ before decreasing again.

plume model. As emission field we use the CO_2 city emission inventories of Munich and Paris from Sec. 3. Figure 5 depicts the relative errors of the SR in the spatial and wavelet domain and LS estimates of (a) Munich's and (b) Paris's emission fields. Errors of the estimates for both SR in the spatial and wavelet domain decrease with an increasing wind coverage for Munich and Paris. In contrast, the LS estimates reveal no clear improvement for higher wind coverages, but its relative error increases with high coverages for Munich, while for Paris the error initially decreases, until about a coverage of $150°$, before increasing again. A sensitivity analysis, given in Appendix F, reveals that error variations given by the different wind coverages are due to the shift of sensitivity to different parts of the domain, while the sum of the sensitivities do not change.

This major improvement of SR for higher wind coverage can be explained using the incoherence property from CS. The coherence parameter, given in Eq. (11), calculates the maximum similarity of how two emission grid cells are measured. For the spatial domain, by increasing the wind coverage, there is greater variety in the measurements and thus between the

300 measurements of two different grid cells. In the wavelet domain, we determined the coherences at different wind coverages and found a similar behavior. Even though for both domains the coherence for a wind coverage of $360°$ is too high to offer reconstruction guarantees, our example shows that including CS parameters in the design process can improve reconstruction results.

4.2.2 Sparse Reconstruction in the Wavelet Domain

305 In the following, we compare reconstruction results of SR in the wavelet and spatial domains. Accordingly, s sparse city emission fields are used to compare these domains. More precisely, the s highest emitters of the CO_2 inventory of London are used to generate an s sparse emission field. This allows us to determine at which trade-off in sparsity the wavelet domain can achieve better results compared to the spatial domain. We chose the inventory of London, since it has the emission field with the lowest compressibility (see table 2).

(a) $\frac{m}{n} \approx 50\ \%$ (b) $\frac{m}{n} \approx 75\ \%$
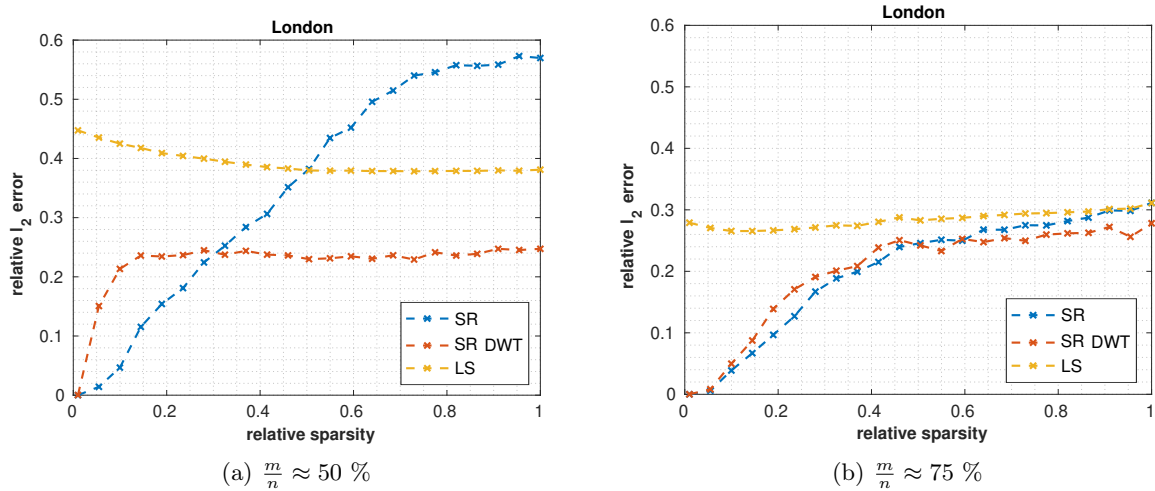
Figure 6. Comparison of the LS (yellow) and SR in the spatial (blue) and wavelet (red) domains in terms of relative sparsity s_{rel}. An emission map artificially generated from London's emission inventory with a total of 2205 unknown emitters was used. The x-axis represents the portion of these emitters that were used (the emitters are sorted from large to small). In (a) 22 measurement stations with a total of 1100 measurements and (b) 33 measurement stations with a total of 1650 measurements are used.

310 Figure 6 shows the relative reconstruction error in the spatial and 3$^{\mathrm{rd}}$ level wavelet domain for different sparsity levels using $\frac{m}{n} \approx 50\ \%$ and $\frac{m}{n} \approx 75\ \%$. As expected, SR in the spatial domain performs better for sparse emission maps (low s). For less sparse emission maps (higher s), however, the wavelet domain is superior.

With fewer measurements, the error in the wavelet domain already plateaus for $s_{\mathrm{rel}} \approx 15\ \%$, while for $\frac{m}{n} \approx 75\ \%$ the error plateaus at $s_{\mathrm{rel}} \approx 40\ \%$. The results also indicate that for the entire emission map of London ($s_{\mathrm{rel}} = 1$), the performance of SR in 315 the wavelet domain does not increase significantly when the measurements are changed from $\frac{m}{n} \approx 50\ \%$ to $\frac{m}{n} \approx 75\ \%$, while the performance in the spatial domain benefits considerably. This improved performance is caused by the higher compressability

of the emission map in the wavelet domain, where the highest wavelet coefficients already provide a good representation of the entire emission map, while the spatial domain needs more coefficients for a representation with the same relative error. Therefore, the wavelet domain requires fewer measurements compared to the spatial domain, to achieve the same performance

320 for cities with emission fields that have a low compressibility (for similar results see section 4.3.3).

Our result demonstrates that the wavelet domain can help to improve SR in those instances for which the spatial domain is not well suited. However, changing the domain also alters the conditions of CS; therefore, conclusions made for CS in the spatial domain can not be directly transferred to the wavelet domain. For example, while a higher wind coverage is beneficial for the spatial domain, such might not be the case for the wavelet domain.

325 **4.2.3 Discovering Unknown Emitters**
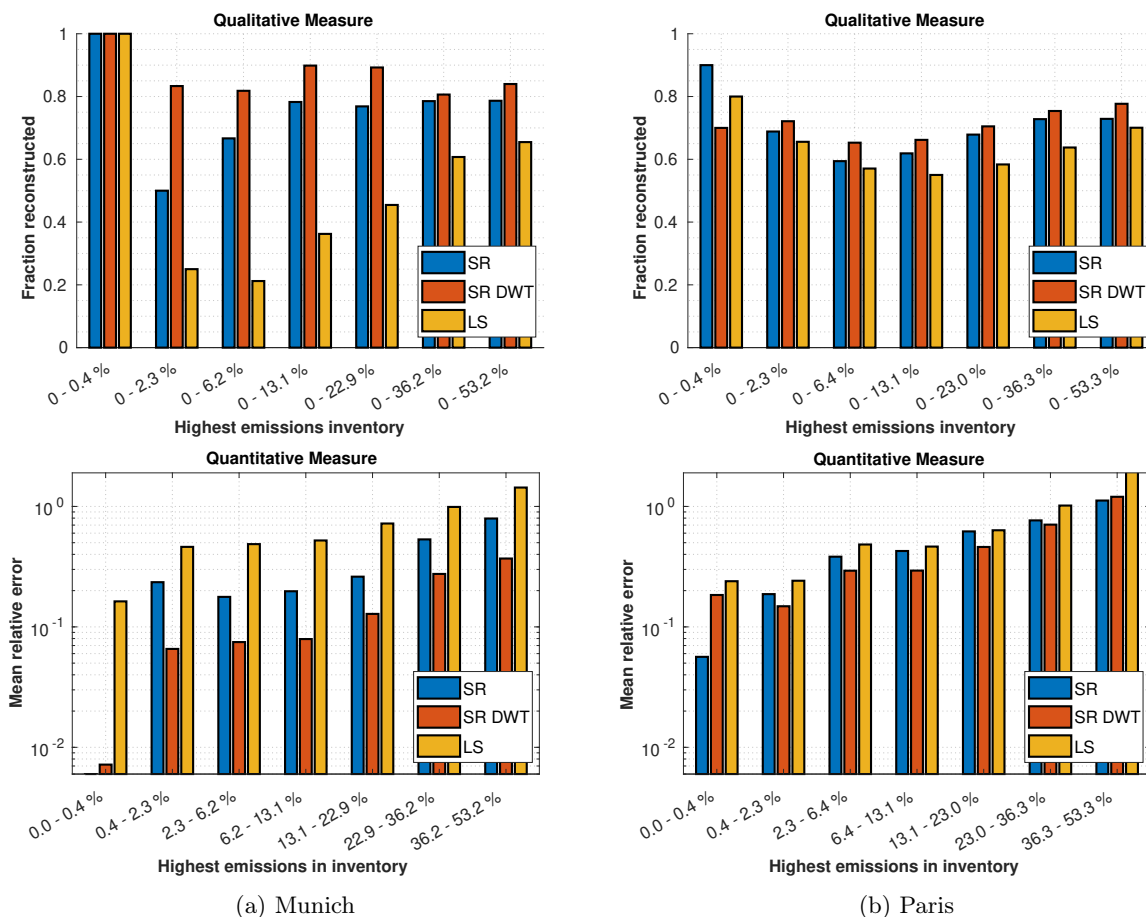
(a) Munich   (b) Paris

Figure 7. Qualitative and quantitative measure of how well SR and LS estimate the highest emissions for (a) Munich and (b) Paris.

In the following, we evaluate how well SR can identify unknown emitters. Assuming a good prior estimation of the emission field, where the relative error for the real emissions for each emitter is approximately constant and small, unknown emitters can be assumed to make a huge contribution to the difference between the prior expected measurements and real measurements. Therefore, we evaluate how well the highest emitters are reconstructed to assess the performance of finding unknown emitters.

To do this, we consider the emission inventory data for Munich and Paris. While Munich's emissions inventory is highly compressible, the emission inventory of Paris is not. For the setup, seven measurement stations are used in Munich and 39 in Paris. This results in $\frac{m}{n} \approx 75\%$ for both cities, making the estimation results comparable.

We employ a qualitative and a quantitative measure, both of which are depicted in Fig. 7. The x-axes show bins of emission grids ranked by their emission strength. For example, the first bin (0 - 0.4%) contains the first 0.4% highest emission grids, while the last bin in the lower panels of Fig. 7 contains emission grids which are among the $36.2-53.2\%$ highest emission grids. Since the emissions have a high compressibility (the first highest emissions make a huge contribution to the total emissions), we use a logarithmic scale for the bins.

The qualitative measure (see upper panels in Fig. 7) compares the fraction of the highest emitters in the inventory matching with those of the estimation (the higher ratio, the better). In Munich, all three methods reconstruct the same largest 0.4% emitters. For Paris, SR in the spatial domain performs best followed by the LS in case of the largest 0.4% emitters. For lower emitters, SR in the wavelet domain performs best for both cities. While the performance gain of SR and SR DWT over the LS method is quite large in Munich, which has a highly compressible emission inventory, the gain is smaller in Paris, which has a slightly compressible inventory.

The quantitative measure (see lower panels in Fig. 7) compares the relative error in the reconstructed emissions (the lower, the better).

For the largest 0.4% emitters, SR in the spatial domain performs best and can reconstruct these emissions with an error less than 0.7% in Munich and 3% in Paris. When analyzing slightly lower emissions, SR in the spatial domain performance drops significantly and the wavelet domain performs best in both cities.

The results indicate that SR in the spatial domain works particularly well for the highest emitters (largest 0.4% in our examples), while SR in the wavelet domain performs well for a broader range of high emitters. The LS performance is much less sensitive to the emission strength of individual strong emitters, which is not beneficial for estimating large unknown emitters.

These results for the same scenario but with fewer measurement stations ($\frac{m}{n} \approx 50\%$) can be found in Appendix D.

4.2.4 Number of Measurements needed

Previous scenarios have presented comparisons between SR and LS using $\frac{m}{n} \approx 50\%$ or $\frac{m}{n} \approx 75\%$. However, the question of how many measurements m are needed to produce results of a certain accuracy remains unanswered. To determine this, we vary the number of measurements per station, which leads to a variation of $\frac{m}{n}$.

Figure 8 depicts the relative estimation error for Munich and Paris for varying $\frac{m}{n}$. In Munich, where the emissions are highly compressible, the reconstruction error for SR in the spatial domain already drops sharply for $\frac{m}{n} \gtrsim 10\%$. SR in the wavelet
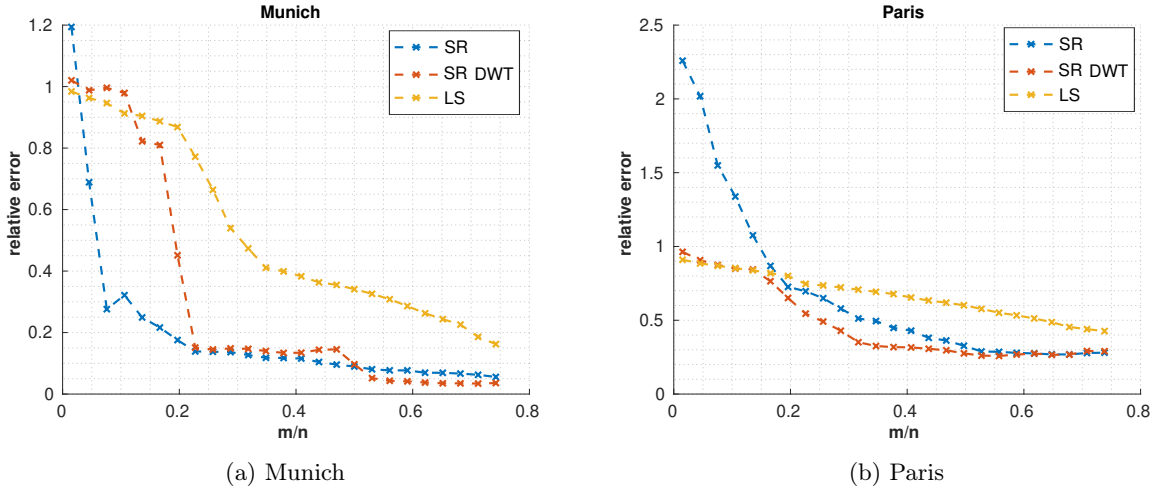
Figure 8. relative error for SR, SR with DWT, and LS at different degrees of undersampling, for (a) Munich and (b) Paris.

domain needs more measurements but performs similar to the spatial domain using $\frac{m}{n} \gtrsim 23$ % and performs even slightly better than the spatial domain for $\frac{m}{n} > 50$ %. The LS also sees a steep improvement with $\frac{m}{n} \approx 30$ %, but does not produce results as good as SR.

For Paris, where the emissions have a low compressibility, SR in the spatial domain performs worst for $\frac{m}{n} < 20$ % while the wavelet domain performs about the same as the LS for this number of measurements. For a higher number of measurements ($\frac{m}{n} > 0.2$), both SR methods show increased performance and both perform better than the LS. Overall, SR in the wavelet domain performs best.

These trends are also confirmed for the emissions of other cities (see supplement). These results demonstrate that when using SR instead of the LS, a higher undersampling with fewer errors is possible, especially for highly compressible emissions (as in Munich).

4.2.5 Measurement Noise

To make the results applicable to real world scenarios, noise has also to be taken into consideration. There are different types of noise, including measurement noise, transport error, and representation error. In the following, we assume measurement errors with an SNR typical for column measurements. Chen et al. (2016) reports measurement errors for column measurements for an average time of 10 minutes for CO_2 as 0.04 to 0.05 ppm and for CH_4 as 0.2 ppb. Jones et al. (2021) shows that CH_4 concentration enhancements measured for the city of Indianapolis are in the order of several ppb. Below, we assume an SNR of 20 dB which corresponds to enhancements of 2 ppb for methane or 0.4 to 0.5 ppm for CO_2. As emission fields, we use the inventory data for Munich. Compared to the noiseless case, we increase the number of measurement stations to $\frac{m}{n} \approx 1.5$, which are 15 measurement stations with a total of 750 measurements. Figure 9 depicts how the relative l_2 error changes for different SNRs in the Munich simulation. The figure shows that the results we obtain for an SNR of 20 dB should not differ significantly
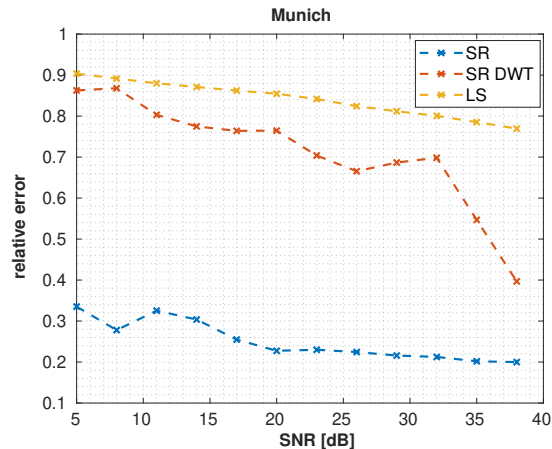
Figure 9. Reconstruction errors of SR in the spatial and wavelet domain as well as LS for Munich when varying the SNR and $\frac{m}{n} \approx 1.5$.

380   for slightly lower or higher SNRs, between 15 dB and 25 dB. Therefore, we believe that despite our noise assumptions which are optimistic compared to real world scenarios, our results are qualitatively valid. We provide a variance map for SR with an SNR of 20 dB in Appendix E. Here, we show the relative error of the estimated emission fields for the noisy case at different
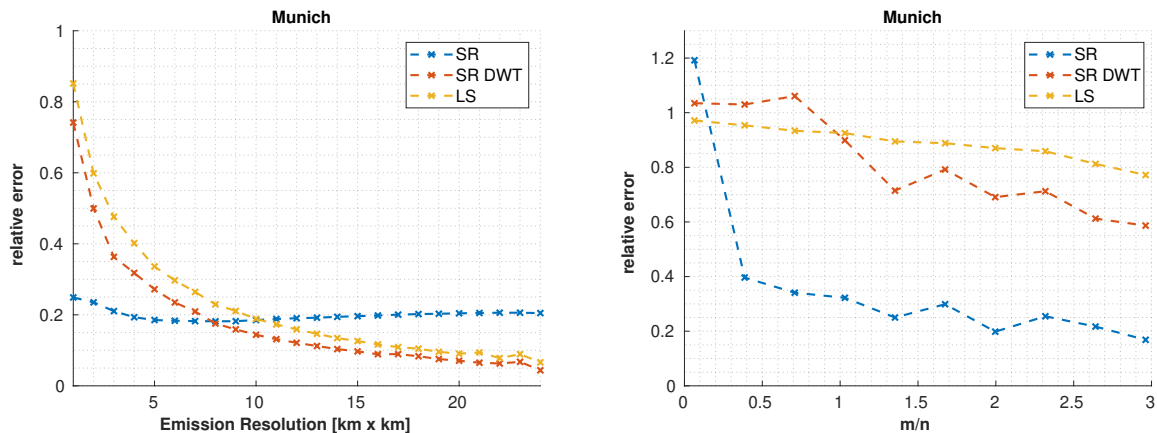
Figure 10. Reconstruction errors uses SR in the spatial and wavelet domain as well as the LS for Munich with an SNR of 20 dB where (a) shows the average relative error for the reconstruction on 250 different noise vectors at different levels of resolutions using $m/n \approx 1.5$ and (b) the relative error for the highest resolution (1 km $\times$ 1 km) when varying the number of measurements.

spatial resolutions of the emissions, both for SR in the spatial domain and wavelet domain and for the LS (see Fig. 10, left). For this case we have run the reconstruction on 250 different noise vectors and show the mean estimation result. Furthermore, we

385   assess the undersampling capability in the noisy case (see Fig. 10, right). For SR in the spatial domain, the relative error is only slightly higher for high resolutions and remains fairly constant across other spatial resolutions, suggesting that almost all errors

occur in the reconstruction of emission strength rather than in the localization of emitters. Both SR in the wavelet domain and the LS have a high relative error for high resolutions (below 7 km × 7 km), while at lower resolutions both perform better than SR in the spatial domain, indicating that most of the error is due to incorrect localization of emitters.

390   As a result, they do not provide accurate localization of the emitters. To overcome this, more measurements are needed for SR in the wavelet domain and LS. To determine the number of measurements required, we show the relative errors for the highest resolution (1 km × 1 km) when varying the number of measurements in Fig. 10 (b). For SR in the spatial domain, the relative error drops significantly for $\frac{m}{n} < 50$ % and performs better than the other reconstruction methods for more measurements. The wavelet domain performs similar to the LS for $\frac{m}{n} < 1$ and better for $\frac{m}{n} > 1$. These results indicate that SR in the spatial

395   domain, for Munich, is more robust against noise, while the wavelet domain is not as robust (many more measurements are needed than in the noiseless case for similar results).
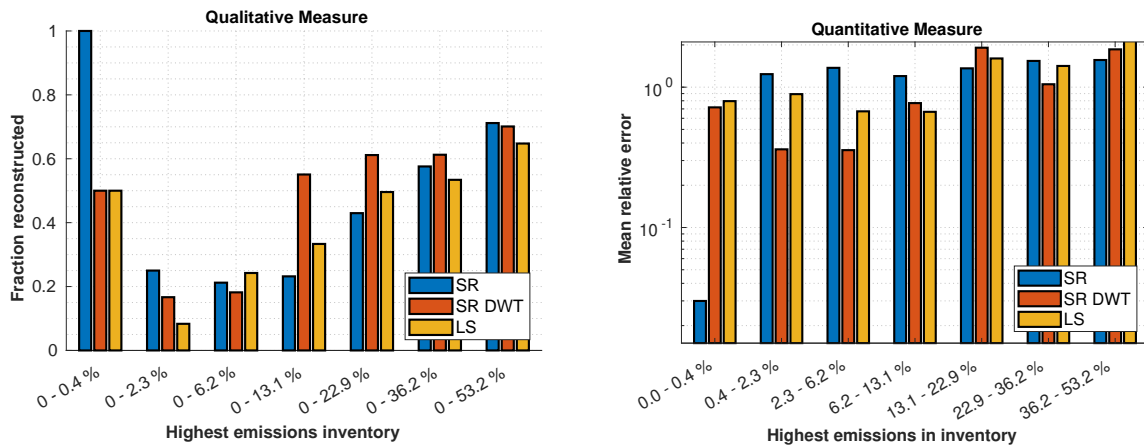
Figure 11. Qualitative and quantitative measure of how well SR and LS estimate the highest emissions with noise of 20 dB for Munich. The qualitative plot shows how many percents of the highest emissions in the inventory are also contained in the same highest amount of emission of the reconstruction. The quantitative plot shows the mean relative errors for different emission strengths.

Next, we analyze the performance of finding unknown emitters in the noisy case. For this purpose, we use the same setup as in Sec. 4.2.3 but solely look at the emissions in Munich. We again use $\frac{m}{n} \approx 1.5$ and add the noise with an SNR of 20 dB. We employ a qualitative and a quantitative measure, both of which are depicted in Fig. 11 (for the description of the measures, see

400   Sec. 4.2.3). SR is the only method to identify the 0.4 % highest emitters (qualitative measure) and estimates their emissions with a significantly lower relative error of 2 % (quantitative measure). Slightly smaller emitters are better estimated by the SR in the wavelet domain. For even lower emitters, there is no clear winner of which method estimates them best. Compared to the noiseless case, the estimation errors are in general larger and SR in the wavelet domain does not achieve as promising results as in the noiseless case. SR in the spatial domain remains sensitive to the largest emitters in the noisy case. These results for

405   Paris are found in the supplement.

5 Broader Comparison of Sparse Reconstruction for European Cities

In the following, case studies on emission fields of all cities considered in Sec. 3 are introduced to more broadly compare the performance of SR. The measurement configuration corresponds to the specifications in Sec. 4.1. The emissions are reconstructed using SR in the spatial and wavelet domains as well as the LS, first with $\frac{m}{n} \approx 75\,\%$ in the noiseless case and then with $\frac{m}{n} \approx 1.5$ in the noisy case. To compare the performance, we measure relative errors, relative smoothed errors (for a spatial

Table 3. Reconstruction performances for SR in the spatial and wavelet domain as well as for LS by measuring the relative error (1 km × 1 km), relative smoothed error (5 km × 5 km), and the relative total error for different European cities. The best approach for each city and type of error is highlighted in gray.

Case study	relative total error			relative smoothed error (5 km × 5 km)			relative error (1 km × 1 km)		
	SR	SR DWT	LS	SR	SR DWT	LS	SR	SR DWT	LS
slightly compressible									
London	0.0 %	0.9 %	0.0 %	4.5 %	4.3 %	4.2 %	32.2 %	27.8 %	31.5 %
Paris	0.0 %	1.4 %	0.0 %	4.4 %	6.4 %	6.7 %	27.4 %	29.4 %	43.2 %
highly compressible									
Berlin	0.0 %	0.7 %	0.2 %	2.2 %	2.7 %	18.5 %	8.1 %	8.1 %	59.0 %
Hamburg	0.0 %	1.0 %	0.4 %	1.9 %	2.3 %	15.0 %	8.2 %	8.8 %	62.2 %
Munich	3.1 %	1.3 %	4.3 %	3.5 %	2.4 %	10.9 %	6.1 %	3.9 %	26.2 %
Vienna	2.2 %	1.5 %	1.3 %	4.9 %	3.2 %	13.0 %	6.9 %	6.2 %	48.8 %

resolution of 5 km × 5 km), and relative total errors. The results for the noiseless case are in Table 3. At the highest spatial resolution (1 km × 1 km, right column in Table 3), SR performs much better than LS for the highly compressible emission fields in both domains. For the cities with emission fields that are slightly compressible, the SR performance is significantly worse than the other cities but still slightly better than LS. For a lower spatial resolution of 5 km × 5 km (middle column in Table 3), the error of all methods decreases. Among the highly compressible emissions, SR still performs significantly better than LS. Both for London and Paris (slightly compressible), all methods produce a similar error, with the LS giving the smallest error in London and SR in the spatial domain giving the smallest error in Paris. For the total emissions, all reconstruction methods perform similarly.

These results support our previous findings that SR performs well at high resolutions for cities with highly compressible emissions.

Next, we consider the noisy case with an SNR of 20.0 dB and $\frac{m}{n} \approx 1.5$ (see the results in Table 4). For the cities that are slightly compressible, SR in the spatial domain performs the worst, while SR in the wavelet domain and the LS perform similarly.

For the highly compressible cities, SR in the spatial domain produces the best results for the 1 km × 1 km and 5 km × 5 km resolution and is worse than the other reconstruction methods for the total emissions (except for Vienna). Furthermore, SR

Table 4. Reconstruction performances for SR in the spatial and wavelet domain as well as for LS by using $\frac{m}{n} \approx 1.5$ with an SNR of 20.0 dB for different European cities. The results are evaluated using the relative error (1 km × 1 km), relative smoothed error (5 km × 5 km), and the relative total error. The best approach for each city and type of error is highlighted in gray.

Case Study	relative total error			relative smoothed error (5 km × 5 km)			relative error (1 km × 1 km)		
	SR	SR DWT	LS	SR	SR DWT	LS	SR	SR DWT	LS
slightly compressible									
London	12.5 %	1.6 %	2.2 %	38.4 %	19.9 %	19.9 %	162.3 %	81.7 %	81.6 %
Paris	11.8 %	2.2 %	1.9 %	32.5 %	24.0 %	24.4 %	144.4 %	83.9 %	83.1 %
highly compressible									
Berlin	10.6 %	0.1 %	1.3 %	18.0 %	29.0 %	32.6 %	36.5 %	85.3 %	85.8 %
Hamburg	10.1 %	1.2 %	1.5 %	20.7 %	32.7 %	34.1 %	70.3 %	88.2 %	87.0 %
Munich	19.3 %	2.6 %	5.6 %	16.9 %	23.6 %	32.8 %	21.4 %	70.8 %	84.2 %
Vienna	11.2 %	21.6 %	6.3 %	20.2 %	61.5 %	41.4 %	38.9 %	96.7 %	92.3 %

in the wavelet domain performs better than the LS. In contrast to the noiseless case, SR in the wavelet domain performs worse than SR in the spatial domain for high resolutions ($\lesssim$ 5 km × 5 km). Both results support our findings from Sec. 4.2.5, that SR in the spatial domain accurately localizes emissions and that SR in the wavelet domain is not as robust to noise as the spatial domain for high resolutions.

6 Conclusions

In this paper, we introduced sparse reconstruction (SR) as a novel method for the inversion of urban GHG emissions, and further provided key examples to identify the advantages of SR to inversely model emissions.

SR can be easily integrated into existing top-down frameworks for estimating emission. We examined the applicability of this method by evaluating the sparseness of emissions from several European cities. Our results indicate that the emissions from most of these cities are sparse and that SR is applicable. We also showed that a wavelet transform increases the sparsity of urban emissions, making SR applicable to cities with less sparse emissions. SR is known to have reconstruction guarantees if conditions of compressed sensing (CS) are satisfied. We tested different CS conditions for various wind fields and showed that wind fields with better CS conditions do significantly increase the performance of SR.

Compared to state-of-the-art inversion methods using Gaussian priors, our method requires fewer measurements and provides better localization and quantification of unknown emitters.

SR works best if the underlying representation of the emissions is sparse. In this paper, we employed the wavelet transform to increase the sparsity; however, other transformations, such as a curvelet transform or more general dictionary representations, might be even more suited for specific spatial domains. Finding such transformations which also work well with CS conditions is challenging, and future studies should be devoted to them.

445 *Code and data availability.* The code for this paper (Zanger et al., 2022b) is written in Matlab 2021a and available on GitHub: https://github.com/tum-esm/recovery_of_sparse_urban_greeenhouse_gas_emissions (last access: 25 January 2022). The Gaussian plume footprints are available at https://doi.org/10.5281/zenodo.5901298 (Zanger et al., 2022a). The TNO_GHGco_v1.1 emission inventory (van der Gon et al., 2019) is not publicly available. The latitude and longitude boundaries used to generate the city emission fields from the inventory is given in Appendix A.

450 *Acknowledgements.* We would like to thank Alihan Kaplan from the chair of Theoretical Information Technology for his comments and useful discussions. We also like to thank Dr. Stephen Starck for helping us to improve the language in the paper. We are thankful to the editor and reviewers for their careful revision and the useful comments and suggestions they provided to improve the paper. BZ, JC, FD are supported by the Deutsche Forschungsgemeinschaft (DFG, German Research Foundation) (grant nos. CH 1792/2-1, INST 95/1544).

Appendix A: Boundaries of the emission inventories

Table A1. Longitude and latitude boundaries used to create the CO_2 emission inventories for the European cities from the TNO_GHGco_v1.1 emission inventory.

City	Southernmost latitude	Northernmost latitude	Westernmost longitude	Easternmost longitude
slightly compressible				
London	51.30°	51.70°	-0.52°	0.21°
Paris	48.62°	49.10°	1.94°	2.66°
highly compressible				
Berlin	52.34°	52.68°	13.07°	13.66°
Hamburg	53.37°	53.71°	9.67°	10.27°
Vienna	48.07°	48.31°	16.12°	16.52°
Munich	48.06°	48.25°	11.36°	11.72°

455   Table A1 shows the longitude and latitude boundaries used to create the CO_2 emission fields for the European cities from the TNO_GHGco_v1.1 emission inventory.

Appendix B: Wind fields and Generation of the Sensing Matrix

The sensing matrices we use consist of vectorized footprints generated by the Gaussian plume model with artificial wind data. The Gaussian plume model provides a good enough approximation for Lagrangian particle dispersion models for the purpose

460 of this paper. The footprints are generated for a high resolution grid using a dynamic Gaussian plume with varying wind speed, direction and diffusion. The footprints are then scaled to the domain size of the city. Because of the scaling, the wind speed and

diffusion changes for each city. Nevertheless, we think that this approach makes the reconstruction performances for different cities more comparable than using different footprints for every city.

For Sec. 4.2.1, we use a static Gaussian plume model to generate footprints for different wind coverages. This allows us to ignore additional effects from the dynamical case, for example, in the dynamic case the change in the wind direction produces spiral looking footprints. These footprints have a different shape compared to the footprints generated using a static Gaussian plume model . By using a static model, the footprints are more predictable and systematic, which makes the results of different wind coverages more comparable to each other.

(a) STILT   (b) Gaussian Plume
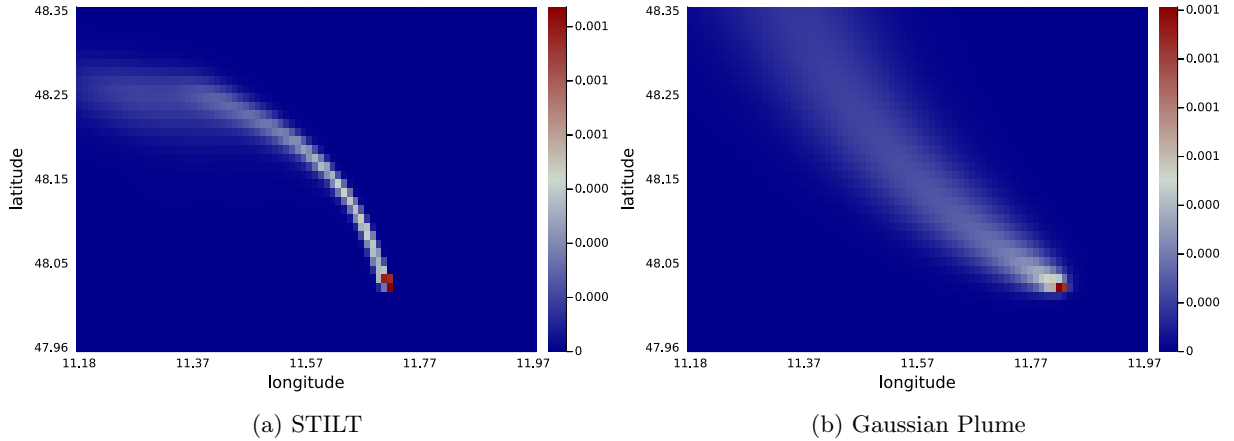
Figure B1. Comparison of a STILT footprint to a Gaussian plume footprint, where different wind fields have been used.

Fig. B1 shows a comparison between a STILT footprint for Munich and a Gaussian Plume footprint used in our work, where the two footprints are generated using different wind fields.

Appendix C: Recovery of Sparse Emissions

Consider s emitters producing an s sparse emission field in a city. We distribute these emitters over the city using a Gaussian distribution, such that the probability for an emitter in the center of the city is higher compared to outside of the city. Furthermore, we use a Gaussian distribution to model the emission strength of each emitter with a mean value of $10\,\mu\mathrm{mol}\cdot(\mathrm{m}^2\cdot\mathrm{s})^{-1}$ and a standard deviation of $1\,\mu\mathrm{mol}\cdot(\mathrm{m}^2\cdot\mathrm{s})^{-1}$, so that all emitters have roughly a similar contribution to the total emissions. In Fig. C1, the reconstruction errors for the spatial domain using SR and LS are depicted. SR allows exact recovery for $s_{\mathrm{rel}} \lesssim 13\,\%$ non zero emissions using $\frac{m}{n} \approx 50\,\%$ and $s_{\mathrm{rel}} > 35\,\%$ non zero emissions using $\frac{m}{n} \approx 75\,\%$. In contrast, the relative error of LS is generally much higher, but decreases with a larger number of measurements.

These results demonstrate the power of SR for sparse emission fields and illustrate the link between SR and CS. As shown in Sec. 2.4, the sensing matrix A must satisfy some sufficient conditions to ensure that CS yields the best possible reconstruction. However, in real-world scenarios, it is challenging to verify these conditions. By using a Monte-Carlo algorithm, we found

(a) $\frac{m}{n} \approx 50\ \%$ (b) $\frac{m}{n} \approx 75\ \%$
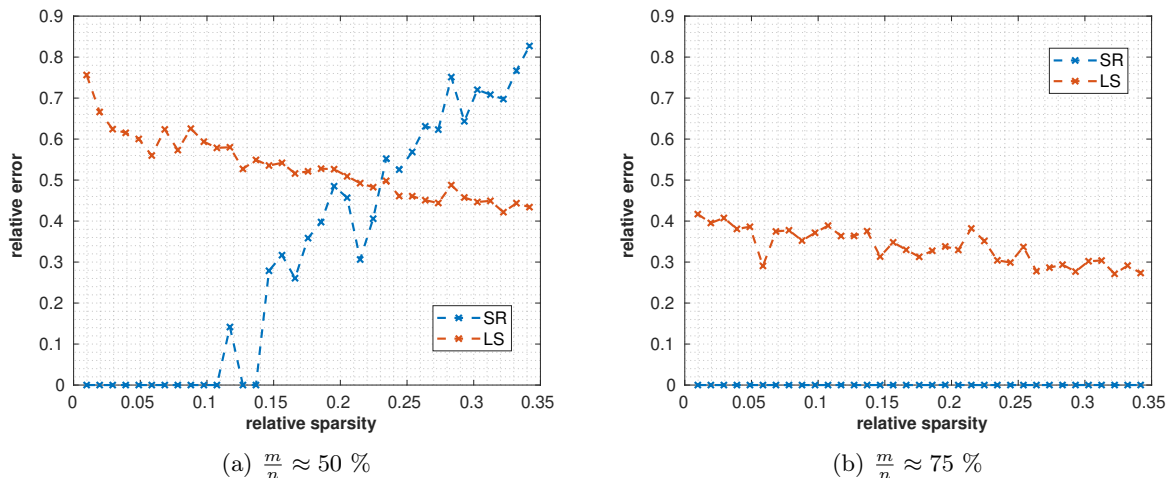
Figure C1. Reconstruction errors for sparse cities with (a) 50 % and (b) 75 % measurements m per emission fields n. Using SR (blue line), it is possible to reconstruct sparse emissions. By increasing the number of measurement stations, and therefore observations, more emitters can be reconstructed using SR (left: up to 13 %; right: up to 35 % non-zero emission cells). For the LS method (red line), the relative error decreases both for less sparse signals and with a larger number of observations.

counterexamples that showed $\delta_{2s} > 1$ for already small s (both for Gaussian Plume footprints and STILT footprints). Thus, the sensing matrix we use here does not guarantee CS for all cases. Nevertheless, A can be useful if it satisfies the CS conditions for some specific emission distributions of interest.

485   Next, we consider the case with $\frac{m}{n} \approx 75\ \%$ and chose a number of emitters s, such that the relative error produced by SR and the LS is similar. Therefore, both methods produce the same relative error, which allows us to compare the spatial distribution of the error on an equal basis. This is the case for $s_{\mathrm{rel}} = 46.9\ \%$, where the relative error for SR is $28.1\ \%$ while the relative error for LS is $27.3\ \%$. We focus on the following questions:

- which emitters are found correctly (discovered)?

490   – which emitters are not found (undiscovered)?

- which emitters are discovered, even though there is no emitter there (false discovered)?

Figure C2 depicts the discovered, not discovered, and falsely discovered emitters for SR (left) and LS (right). SR reconstructs most emitters correctly, only $1.1\ \%$ of the emitters are undiscovered (yellow) and $8.0\ \%$ are falsely discovered (dark blue). In contrast, the LS has no emitters which have not been found, but $45.6\ \%$ falsely discovered emitters. This is because the LS

495   prefers smooth estimates, which is equivalent to estimating emitters everywhere. This is also seen by the fraction between the emissions estimated for falsely discovered emitters and the total estimated emissions. While this fractions is only $3.0\ \%$ for SR, for LS this fraction is $12.2\ \%$.

(a) SR (b) LS

☐ undiscovered ■ false discovered ■ discovered
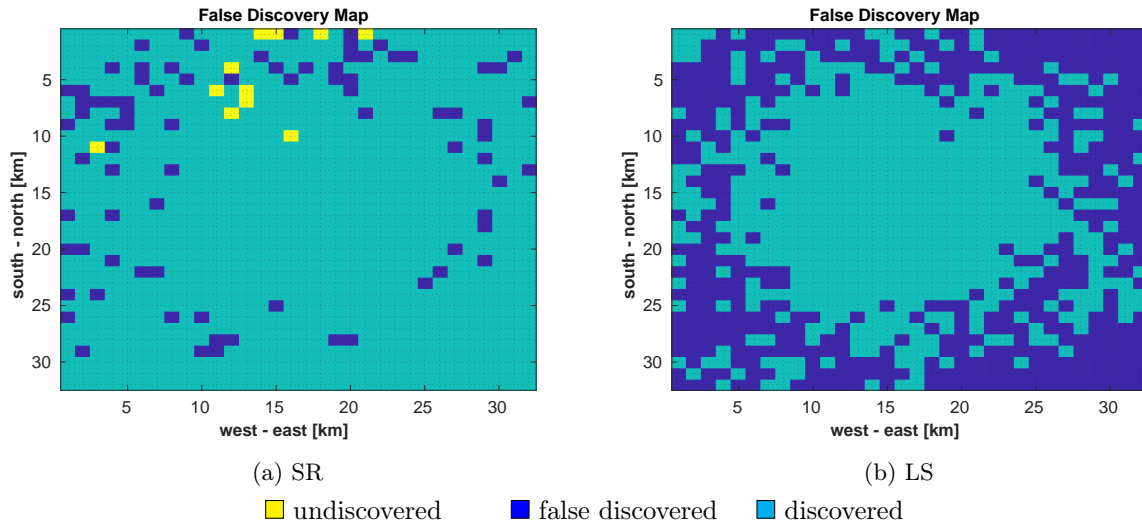
Figure C2. Visualization of false discovered (dark blue), undiscovered (yellow), and discovered (cyan) emissions in x by (a) SR and (b) LS.

These results demonstrates the advantage of SR for the localization of emitters. This property is especially useful to find unknown emitters, since the spatial certainty of emitters for SR is much higher.

500 Appendix D: Discovering unknown emitters using less measurements

In Sec. 4.2.3 we showed that SR is better in finding high emitters compared to LS and can reconstruct those with smaller errors. This is visualized by the Fig. 7 which has been creates using $\frac{m}{n} \approx 75$ %. In the following, we resemble this result using only $\frac{m}{n} \approx 50$ %.
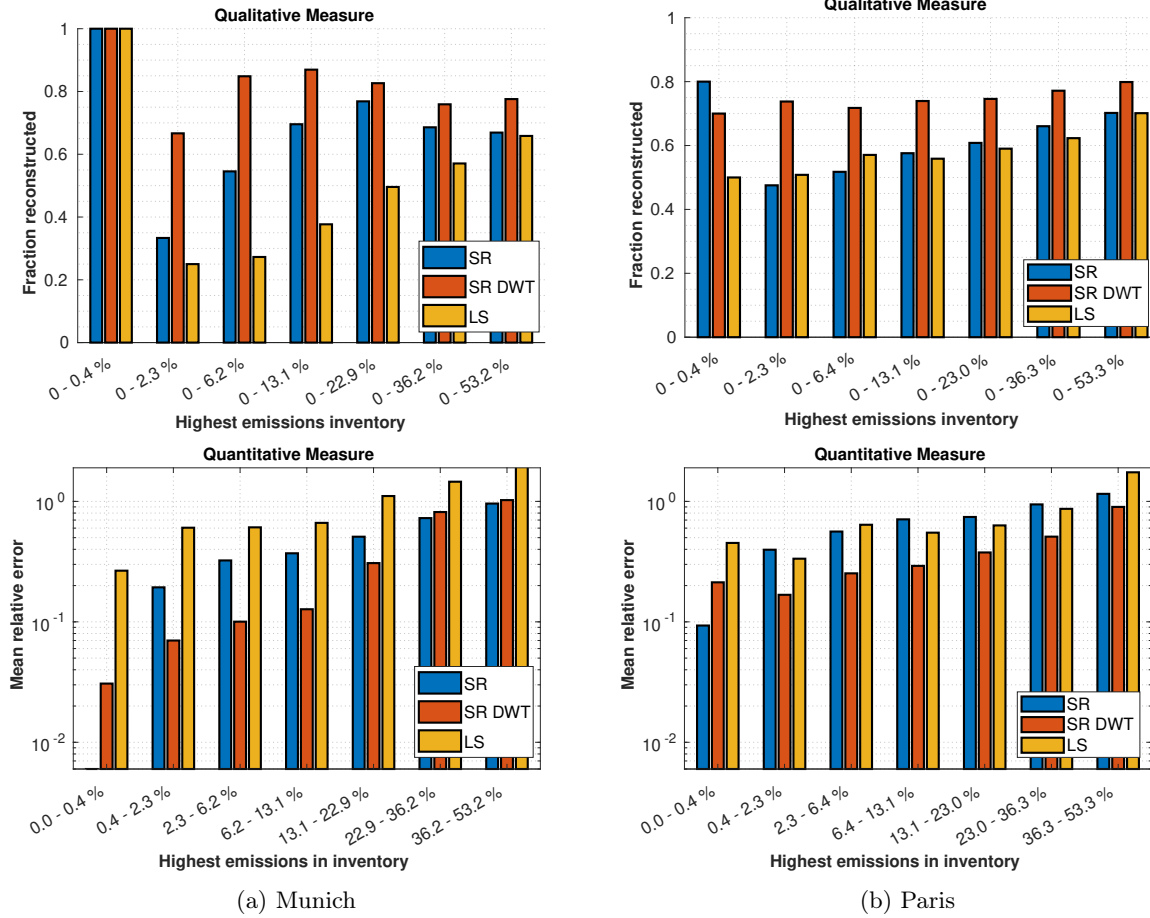
Figure D1. Qualitative and quantitative measure of how well SR and LS estimate the highest emitters for Munich (a) and Paris (b) using $\frac{m}{n} \approx 50$ %.

The results are depicted in Fig. D1. Compared to the case with more measurements, for Munich, SR in the spatial domain performs better in the qualitative measure compared to the wavelet domain. Furthermore, for Paris, the margin between the performance of SR in the wavelet domain and the other methods has increased.

Appendix E: Uncertainty Quantification

Uncertainty quantification for sparse reconstruction is distinct different compared to uncertainty quantification for LS reconstruction. First, while for the LS fit with Gaussian noise a closed form solution exists, there doesn't exist any closed form solution for sparse reconstruction.

In the following we use the uncertainty quantification approach from Hase et al. (2017) in order to derive a variance plot of the reconstruction result by applying bootstrapping. This gives us the covariance matrices for SR in the spatial and wavelet

domain. We only use the variances of the matrix and plot the standard deviations for every single reconstructed emission, which is depicted in Fig. E1. For the spatial domain, the standard deviation is localized around certain areas in the map, while for the

515   wavelet domain, the standard deviation covers much larger areas of the map. This let one believe that a reconstructed emission in the spatial domain has a higher certainty of location compared to SR in the wavelet domain. This assumption is verified by Fig. 10

(a) Spatial domain   (b) Wavelet domain
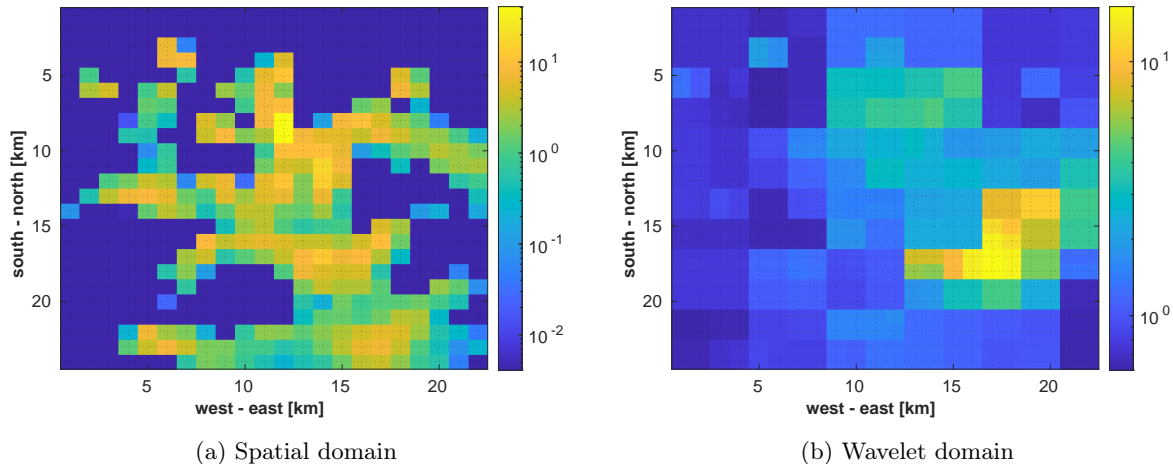
Figure E1. Uncertainty of the emission estimates for Munich with $\frac{m}{n} \approx 1.5$ and an SNR of 20 dB for SR in the (a) spatial domain and (b) wavelet domain.

Appendix F: Least Square sensitivity for different wind coverages

In the following, we are showing that the changes of relative error for LS in sec. 4.2.1 are due to the fact that the sensitivity

520   to different areas of the map changes, while the total sensitivity does not change. Figure F1 depicts the sensitivity map of Munich for a wind coverage of (a) 72° and (b) 360°. For 72°, the south-east is well sensitive to the estimation, while other parts, especially the west of the city, are weakly sensitive. For 360°, there is no area in the city which is not sensitive to the estimation. However, some areas are less sensitive than in the 72° case, especially the south-east. If we compare this sensitivity map to the emission map of Munich in Fig. 4, we see that the strongest emitter is positioned in the south-east. This explains

525   why for the case of 72°, the relative error of the LS is lower than for the 360° case. If we look at the mean sensitivity of an emission grid cell for both cases, we find that those are exactly the same, 0.6629, and a change in wind coverage does not improve the total sensitivity.

(a) Spatial domain   (b) Wavelet domain
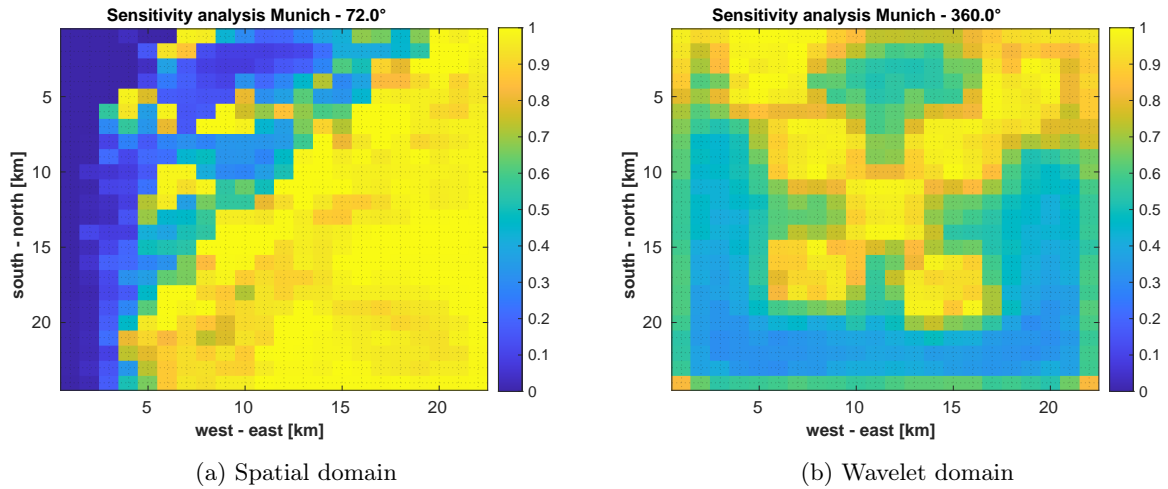
Figure F1. Sensitivity map of LS in Munich for a wind coverage of (a) 72° and (b) 360°. In (a), the south-east is well sensitive to the estimation, while the west and north of the city is only weakly sensitive. In (b), there is no area which is not sensitive to the estimation, but the areas in the south-east are less sensitive.

Author contributions. JC and FD conceived the study; BZ and MS performed the data analysis supervised by JC and FD; BZ, JC and FD wrote the manuscript; BZ and JC revised the manuscript according to the reviewer comments. MS contributed to the content of the manuscript.

530

Competing interests. The authors declare that they have no conflict of interest.

References

Baraniuk, R., Davenport, M., DeVore, R., and Wakin, M.: A simple proof of the restricted isometry property for random matrices, Constructive Approximation, 28, 253–263, https://doi.org/10.1007/s00365-007-9003-x, 2008.

535 Boche, H., Calderbank, R., Kutyniok, G., and Vybíral, J.: A survey of compressed sensing, in: Compressed sensing and its applications, pp. 1–39, Springer, 2015.

Candès, E. J.: The restricted isometry property and its implications for compressed sensing, Comptes Rendus Mathematique, 346, 589–592, https://doi.org/https://doi.org/10.1016/j.crma.2008.03.014, 2008.

Candès, E. J. and Tao, T.: Decoding by linear programming, IEEE Transactions on Information Theory, 51, 4203–4215,
540 https://doi.org/10.1109/TIT.2005.858979, 2005.

Candès, E. J., Romberg, J. K., and Tao, T.: Stable signal recovery from incomplete and inaccurate measurements, Communications on Pure and Applied Mathematics, 59, 1207–1223, https://doi.org/https://doi.org/10.1002/cpa.20124, 2006.

Candès, E. J., Eldar, Y. C., Needell, D., and Randall, P.: Compressed sensing with coherent and redundant dictionaries, Applied and Computational Harmonic Analysis, 31, 59–73, https://doi.org/https://doi.org/10.1016/j.acha.2010.10.002, 2011.

545 Chen, J., Viatte, C., Hedelius, J. K., Jones, T., Franklin, J. E., Parker, H., Gottlieb, E. W., Wennberg, P. O., Dubey, M. K., and Wofsy, S. C.: Differential column measurements using compact
solar-tracking spectrometers, Atmospheric Chemistry and Physics, 16, 8479–8498, https://doi.org/10.5194/acp-16-8479-2016, 2016.

Dietrich, F., Chen, J., Voggenreiter, B., Aigner, P., Nachtigall, N., and Reger, B.: MUCCnet: Munich Urban Carbon Column network, Atmos. Meas. Tech., 14, 1111–1126, https://doi.org/10.5194/amt-14-1111-2021, 2021.

550 Gerbig, C., Lin, J. C., Wofsy, S. C., Daube, B. C., Andrews, A. E., Stephens, B. B., Bakwin, P. S., and Grainger, C. A.: Toward constraining regional-scale fluxes of CO2 with atmospheric observations over a continent: 2. Analysis of COBRA data using a receptor-oriented framework, Journal of Geophysical Research: Atmospheres, 108, https://doi.org/https://doi.org/10.1029/2003JD003770, 2003.

Göckede, M., Turner, D. P., Michalak, A. M., Vickers, D., and Law, B. E.: Sensitivity of a subregional scale atmospheric inverse CO2 modeling framework to boundary conditions, Journal of Geophysical Research: Atmospheres, 115, 2010.

555 Golub, G. H., Hansen, P. C., and O'Leary, D. P.: Tikhonov regularization and total least squares, SIAM journal on matrix analysis and applications, 21, 185–194, 1999.

Grant, M. and Boyd, S.: Graph implementations for nonsmooth convex programs, in: Recent Advances in Learning and Control, edited by Blondel, V., Boyd, S., and Kimura, H., Lecture Notes in Control and Information Sciences, pp. 95–110, Springer-Verlag Limited, http://stanford.edu/~boyd/graph_dcp.html, 2008.

560 Grant, M. and Boyd, S.: CVX: Matlab Software for Disciplined Convex Programming, version 2.1, http://cvxr.com/cvx, 2014.

Graps, A.: An introduction to wavelets, IEEE computational science and engineering, 2, 50–61, 1995.

Gurobi Optimization, LLC: Gurobi Optimizer Reference Manual, https://www.gurobi.com, 2021.

Hase, F., Frey, M., Blumenstock, T., Groß, J., Kiel, M., Kohlhepp, R., Mengistu Tsidu, G., Schäfer, K., Sha, M. K., and Orphal, J.: Application of portable FTIR spectrometers for detecting greenhouse gas emissions of the major city Berlin, Atmospheric Measurement Techniques,
565 8, 3059–3068, https://doi.org/10.5194/amt-8-3059-2015, 2015.

Hase, N., Miller, S. M., Maaß, P., Notholt, J., Palm, M., and Warneke, T.: Atmospheric inverse modeling via sparse reconstruction, Geoscientific Model Development, 10, 3695–3713, https://doi.org/10.5194/gmd-10-3695-2017, 2017.

Hirsch, A. I., Michalak, A. M., Bruhwiler, L. M., Peters, W., Dlugokencky, E. J., and Tans, P. P.: Inverse modeling estimates of the global nitrous oxide surface flux from 1998–2001, Global Biogeochemical Cycles, 20, https://doi.org/https://doi.org/10.1029/2004GB002443, 2006.

Hong, M., Yu, Y., Wang, H., Liu, F., and Crozier, S.: Compressed sensing MRI with singular value decomposition-based sparsity basis, Physics in Medicine and Biology, 56, 6311–6325, https://doi.org/10.1088/0031-9155/56/19/010, 2011.

Jacob, D. J., Turner, A. J., Maasakkers, J. D., Sheng, J., Sun, K., Liu, X., Chance, K., Aben, I., McKeever, J., and Frankenberg, C.: Satellite observations of atmospheric methane and their value for quantifying methane emissions, Atmospheric Chemistry and Physics, 16, 14 371–14 396, https://doi.org/10.5194/acp-16-14371-2016, 2016.

Jones, T. S., Franklin, J. E., Chen, J., Dietrich, F., Hajny, K. D., Paetzold, J. C., Wenzel, A., Gately, C., Gottlieb, E., Parker, H., Dubey, M., Hase, F., Shepson, P. B., Mielke, L. H., and Wofsy, S. C.: Assessing urban methane emissions using column-observing portable Fourier transform infrared (FTIR) spectrometers and a novel Bayesian inversion framework, Atmospheric Chemistry and Physics, 21, 13 131–13 147, https://doi.org/10.5194/acp-21-13131-2021, 2021.

Klappenbach, F., Chen, J., Wenzel, A., Forstmaier, A., Dietrich, F., Zha, X., Jones, T., Franklin, J., Wofsy, S., Frey, M., Hase, F., Hedelius, J., Wennberg, P., Cohen, R., and Fischer, M.: Methane emission estimate using ground based remote sensing in complex terrain, in: Geophysical Research Abstracts of the EGU General Assembly 2021, https://doi.org/10.5194/egusphere-egu21-15406, 2021.

Lewis, A. S. and Knowles, G.: Image compression using the 2-D wavelet transform, IEEE Transactions on image Processing, 1, 244–250, 1992.

Lin, J. C., Gerbig, C., Wofsy, S. C., Andrews, A. E., Daube, B. C., Davis, K. J., and Grainger, C. A.: A near-field tool for simulating the upstream influence of atmospheric observations: The Stochastic Time-Inverted Lagrangian Transport (STILT) model, Journal of Geophysical Research: Atmospheres, 108, https://doi.org/https://doi.org/10.1029/2002JD003161, 2003.

Mallat, S.: A Wavelet Tour of Signal Processing, Elsevier, https://doi.org/10.1016/b978-0-12-466606-1.x5000-4, 1999.

Miller, S. M., Wofsy, S. C., Michalak, A. M., Kort, E. A., Andrews, A. E., Biraud, S. C., Dlugokencky, E. J., Eluszkiewicz, J., Fischer, M. L., Janssens-Maenhout, G., Miller, B. R., Miller, J. B., Montzka, S. A., Nehrkorn, T., and Sweeney, C.: Anthropogenic emissions of methane in the United States, Proceedings of the National Academy of Sciences, 110, 20 018–20 022, https://doi.org/10.1073/pnas.1314392110, 2013.

Mueller, K. L., Gourdji, S. M., and Michalak, A. M.: Global monthly averaged CO_2 fluxes recovered using a geostatistical inverse modeling approach: 1. Results using atmospheric measurements, Journal of Geophysical Research: Atmospheres, 113, https://doi.org/https://doi.org/10.1029/2007JD009734, 2008.

Nakamura, G. and Potthast, R.: Inverse modeling, IOP Publishing, 2015.

Ray, J., Yadav, V., Michalak, A. M., van Bloemen Waanders, B., and McKenna, S. A.: A multiresolution spatial parameterization for the estimation of fossil-fuel carbon dioxide emissions via atmospheric inversions, Geoscientific Model Development, 7, 1901–1918, https://doi.org/10.5194/gmd-7-1901-2014, 2014.

Ray, J., Lee, J., Yadav, V., Lefantzi, S., Michalak, A., and Bloemen Waanders, B. v.: A sparse reconstruction method for the estimation of multi-resolution emission fields via atmospheric inversion, Geoscientific Model Development, 8, 1259–1273, https://doi.org/10.5194/gmd-8-1259-2015, 2015.

Sargent, M., Barrera, Y., Nehrkorn, T., Hutyra, L. R., Gately, C. K., Jones, T., McKain, K., Sweeney, C., Hegarty, J., Hardiman, B., Wang, J. A., and Wofsy, S. C.: Anthropogenic and biogenic CO_2 fluxes in the Boston urban region, Proceedings of the National Academy of Sciences, 115, 7491–7496, https://doi.org/10.1073/pnas.1803715115, 2018.

Shekhar, A., Chen, J., Paetzold, J. C., Dietrich, F., Zhao, X., Bhattacharjee, S., Ruisinger, V., and Wofsy, S. C.: Anthropogenic CO2 emissions assessment of Nile Delta using XCO2 and SIF data from OCO-2 satellite, Environmental Research Letters, 15, 095 010, https://doi.org/10.1088/1748-9326/ab9cfe, 2020.

610   Shusterman, A. A., Teige, V. E., Turner, A. J., Newman, C., Kim, J., and Cohen, R. C.: The BErkeley Atmospheric CO_2 Observation Network: initial evaluation, Atmospheric Chemistry and Physics, 16, 13 449–13 463, https://doi.org/10.5194/acp-16-13449-2016, 2016.

Su, W., Bogdan, M., and Candès, E.: FALSE DISCOVERIES OCCUR EARLY ON THE LASSO PATH, The Annals of Statistics, 45, 2133–2150, http://www.jstor.org/stable/26362897, 2017.

Tibshirani, R.: Regression Shrinkage and Selection via the Lasso, Journal of the Royal Statistical Society. Series B (Methodological), 58, 267–288, http://www.jstor.org/stable/2346178, 1996.

615   Tillmann, A. M. and Pfetsch, M. E.: The Computational Complexity of the Restricted Isometry Property, the Nullspace Property, and Related Concepts in Compressed Sensing, IEEE Transactions on Information Theory, 60, 1248–1259, https://doi.org/10.1109/TIT.2013.2290112, 2014.

Toja-Silva, F., Chen, J., Hachinger, S., and Hase, F.: CFD simulation of CO2 dispersion from urban thermal power plant: Analysis of turbulent Schmidt number and comparison with Gaussian plume model and measurements, Journal of Wind Engineering and Industrial
620   Aerodynamics, 169, 177–193, https://doi.org/https://doi.org/10.1016/j.jweia.2017.07.015, 2017.

Turner, A. J., Jacob, D. J., Wecht, K. J., Maasakkers, J. D., Lundgren, E., Andrews, A. E., Biraud, S. C., Boesch, H., Bowman, K. W., Deutscher, N. M., Dubey, M. K., Griffith, D. W. T., Hase, F., Kuze, A., Notholt, J., Ohyama, H., Parker, R., Payne, V. H., Sussmann, R., Sweeney, C., Velazco, V. A., Warneke, T., Wennberg, P. O., and Wunch, D.: Estimating global and North American methane emissions with high spatial resolution using GOSAT satellite data, Atmospheric Chemistry and Physics, 15, 7049–7069, https://doi.org/10.5194/acp-
625   15-7049-2015, 2015.

Turner, A. J., Kim, J., Fitzmaurice, H., Newman, C., Worthington, K., Chan, K., Wooldridge, P. J., Köhler, P., Frankenberg, C., and Cohen, R. C.: Observed Impacts of COVID-19 on Urban CO2 Emissions, Geophysical Research Letters, 47, e2020GL090 037, https://doi.org/https://doi.org/10.1029/2020GL090037, e2020GL090037 10.1029/2020GL090037, 2020.

van der Gon, H. D., Kuenen, J., Boleti, E., Muntean, M., Maenhout, G., Marshall, J., and Haussaire, J.-M.: Emissions and natural fluxes
630   Dataset, https://www.che-project.eu/sites/default/files/2019-01/CHE-D2-3-V1-0.pdf, 2019.

Viatte, C., Lauvaux, T., Hedelius, J. K., Parker, H., Chen, J., Jones, T., Franklin, J. E., Deng, A. J., Gaudet, B., Verhulst, K., Duren, R., Wunch, D., Roehl, C., Dubey, M. K., Wofsy, S., and Wennberg, P. O.: Methane emissions from dairies in the Los Angeles Basin, Atmospheric Chemistry and Physics, 17, 7509–7528, https://doi.org/10.5194/acp-17-7509-2017, 2017.

Wang, Y., Zeng, J., Peng, Z., Chang, X., and Xu, Z.: Linear convergence of adaptively iterative thresholding algorithms for compressed
635   sensing, IEEE Transactions on Signal Processing, 63, 2957–2971, 2015.

Wesloh, D., Lauvaux, T., and Davis, K. J.: Development of a Mesoscale Inversion System for Estimating Continental-Scale CO2 Fluxes, Journal of Advances in Modeling Earth Systems, 12, e2019MS001 818, https://doi.org/https://doi.org/10.1029/2019MS001818, e2019MS001818 10.1029/2019MS001818, 2020.

Yan, S., Wu, C., Dai, W., Ghanem, M., and Guo, Y.: Environmental Monitoring via Compressive Sensing, in: Proceedings of the Sixth
640   International Workshop on Knowledge Discovery from Sensor Data, SensorKDD '12, p. 61–68, Association for Computing Machinery, New York, NY, USA, https://doi.org/10.1145/2350182.2350189, 2012.

Zanger, B., Chen, J., Sun, M., and Dietrich, F.: Gaussian plume footprints, https://doi.org/10.5281/zenodo.5901298, 2022a.

Zanger, B., Chen, J., Sun, M., and Dietrich, F.: tum-esm/recovery_of_sparse_urban_greeenhouse_gas_emissions: v0.1.0, https://doi.org/10.5281/zenodo.5900738, 2022b.

645 Zonoobi, D., Kassim, A. A., and Venkatesh, Y. V.: Gini Index as Sparsity Measure for Signal Reconstruction from Compressive Samples, IEEE Journal of Selected Topics in Signal Processing, 5, 927–932, https://doi.org/10.1109/JSTSP.2011.2160711, 2011.

©OpenStreetMap contributors 2020. Distributed under the Open Data Commons Open Database License (ODbL) v1.0.: Map data, https://www.openstreetmap.org/copyright, 2020.